Ultrafast Dynamics in Ni and Pt/Fe Bilayer Thin Films

A thesis submitted in partial fulfillment of the requirements for the award of the degree of

BS-MS DUAL DEGREE

by

Abhay Saxena

(21MS086)

Under the supervision of

Prof. Kamaraju Natarajan

(Professor, IISER Kolkata)

to the

Department of Physical Sciences

Indian Institute of Science Education and Research Kolkata

Tuesday 12th May, 2026

Certificate

This is to certify that the thesis titled **"Ultrafast Dynamics in Ni and Pt/Fe Bilayer Thin Films"** submitted by **Abhay Saxena**, registration No.**21MS086**, a student of the Department of Physical Sciences of the BS-MS Dual Degree Programme of IISER Kolkata, is based upon his own research work under my supervision. I also certify, to the best of my knowledge, that neither the thesis nor any part of it has been submitted for any degree/diploma or any other academic award anywhere before. In my opinion, the thesis fulfils the requirement for the award of the degree of **BS-MS Dual Degree**.

N. Kamaraju

Signature

Date: Tuesday 12th May, 2026

Prof. Kamaraju Natarajan
Professor
Department of Physical Sciences
Indian Institute of Science Education and Research Kolkata
Mohanpur 741246, West Bengal, India

Declaration

This is to certify that the thesis titled **"Ultrafast Dynamics in Ni and Pt/Fe Bilayer Thin Films"** has been authored by me. It presents the research conducted by me under the supervision of Prof. Kamaraju Natarajan. To the best of my knowledge, it is an original work, both in terms of research content and narrative, and has not been submitted elsewhere, in part or in full, for a degree. Further, due credit has been given to the relevant state-of-the-art and to collaborations, with appropriate citations and acknowledgments, in line with established norms and practices. I have used the originality checking service to prevent inappropriate plagiarism.

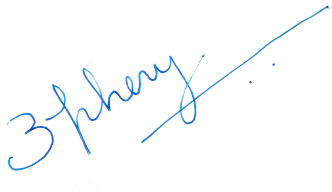

Signature

Date: Tuesday 12th May, 2026

Abhay Saxena
Roll No. 21MS086
5 Year BS-MS Dual Degree
Department of Physical Sciences (DPS)
Indian Institute of Science Education and Research Kolkata
Mohanpur 741246, West Bengal, India

Acknowledgements

I am forever grateful to my parents, Nishu and Jitin Saxena, and my brother, Tanishq. Their unconditional love and belief in me were my primary anchors, providing the strength to navigate these five years whenever challenges arose.

I am especially lucky to have had Prof. Kamaraju Natarajan as my supervisor. He is a truly great teacher who put considerable effort into showing me how to explain physics clearly through various presentations, which helped me immensely during my doctoral applications. He provided me with valuable hands-on experience working with the lab equipment and handling delicate samples, teaching me the responsibility and precision required in experimental work. He made the whole subject of ultrafast dynamics so fascinating that I couldn't help but be drawn into it. I really appreciate his constant guidance, his advice, and the way he pushed us to strive for excellence in our work every day.

I also owe a lot to Sourav Rana Bhaiya. He was always there to guide me in the lab and taught me how to build the entire experiment from the ground up. He was very patient with me while I was learning, and his technical skills were the reason my experiments actually worked.

I want to thank Prof. Sunil Kumar from IIT Delhi for providing the Fe/Pt Spintronic Emitters. I also thank Prof. Partha Mitra and Harekrishna Bhunia for giving me the various Ni samples I needed for my research.

I am deeply grateful to Prof. Kuntal Roy from IISER Bhopal for teaching me how to build experimental setups and how to fix problems until they actually worked. He worked with me every step of the way and taught me the right way to think and keep records in a lab.

A big thank you to Prof. Amit Ghosal for believing in me. His support helped me reach my full potential and grow as a researcher.

Special thanks to my lab mates, Kiran Manoj and Kaustav Roy. We really worked throughout together. I am so grateful for the nights they stayed late in the lab just to help me with my work, even when they had their own projects to finish. Having them there during those long hours made everything much easier.

I also want to thank my lab seniors, namely Anupama Didi, Poulami Didi, Siddhanta Bhaiya and all their encouragement. Their advices really helped me stay on track when I was working in the lab. I also want to thank Krishna Bhaiya for his contributions to the setup.

Finally, I want to thank my friends Ananya, Poluri, Shagnik, and Nimish. They have been with me for this whole five-year journey. They made my life fun and provided the emotional support I needed to finally finish this work.

Abstract

This thesis systematically investigates the fluence-dependent ultrafast energy dissipation in pure Nickel thin films and Fe/Pt spintronic bilayers using femtosecond pump-probe spectroscopy. We observe a fundamental difference in the initial thermalization dynamics between the two systems: the signal rise time remains constant for pure Ni, whereas in the Fe/Pt bilayer, it progressively stretches from approximately 200 fs to 320 fs with increasing pump fluence. Despite this difference in the excitation phase, the subsequent thermal recovery exhibits similar scaling in both systems. All extracted thermal relaxation time constants (τ_1 and τ_2 for Ni; τ_1, τ_2, and τ_3 for Fe/Pt) increase linearly as a function of incident fluence. Furthermore, the signal amplitudes associated with the fast electronic decays (A_1 for Ni; A_1 and A_2 for Fe/Pt) follow a power-law increase, reflecting the nonlinear response of the highly excited electron bath. In contrast, the amplitudes governing the slow thermal recovery tail (A_2 in Ni; A_3 in Fe/Pt) scale strictly linearly with fluence in both systems, representing the classical macroscopic thermal heating of the atomic lattice. These results provide a direct, comparative mapping of the thermodynamic energy transfer channels in pure ferromagnets versus spintronic heterostructures and gives an insight on the role of Pt.

Contents

Chapter 1

Introduction

1.1 Pump-Probe Studies in Metals

The interaction of ultrashort femtosecond laser pulses with metallic solid-state systems has driven immense interest over the past two decades. In transition metals, pump-probe spectroscopy serves as the primary tool to observe highly non-equilibrium physics unfolding on the femtosecond to picosecond timescales [1]. However, depending on the specific optical property being probed, the extracted information differs fundamentally. This often leads to a common question: in a pump-probe experiment on a magnetic metal, are we measuring the structural dynamics or the ultrafast demagnetization?

The answer strictly depends on the detection geometry and polarization. When an intense pump pulse irradiates a metal, it instantly creates a hot, out-of-equilibrium electron bath. If the probe pulse simply measures the transient differential reflectivity ($\Delta R/R$) without polarization sensitivity, it is primarily tracking the thermodynamic evolution of the material's complex dielectric tensor [1]. This $\Delta R/R$ signal maps the initial electron-electron thermalization (T_e) and the subsequent electron-phonon coupling as heat is transferred to the atomic lattice (T_l) [2].

Conversely, if the metal is ferromagnetic, the optical excitation also drastically perturbs the spin subsystem. If the probe pulse is configured to measure polarization rotation via the Time-Resolved Magneto-Optical Kerr Effect (TR-MOKE), the signal tracks the off-diagonal components of the dielectric tensor, providing a direct readout of the ultrafast loss of macroscopic magnetic order (ultrafast demagnetization) [3]. Therefore, normal reflectivity dynamics ($\Delta R/R$) illuminate the charge and lattice cooling pathways, while magneto-optical techniques illuminate the transfer of angular momentum and the evolution of the spin bath (T_s) [3]. Understanding both parallel processes is essential for the burgeoning field of ultrafast THz spintronics.

1.2 Principles of Spintronic Terahertz Emitters

The ability to manipulate electron spins on a sub-picosecond timescale has led to a paradigm shift in the generation of broadband terahertz (THz) radiation. Metallic spintronic THz emitters (STEs), typically consisting of ultrathin ferromagnetic (FM) and non-magnetic heavy metal (NM) heterostructures, have emerged as highly efficient, low-cost, and broadband alternatives to conventional semiconductor-based THz sources [4].

The generation of THz radiation in these FM/NM bilayers (such as Fe/Pt) relies on a sequential, two-part ultrafast process [4]:

1. **Spin Current Generation:** The femtosecond laser pulse excites the FM layer, generating a non-equilibrium electron distribution. Due to the asymmetry in velocities and lifetimes between majority and minority spins, a sub-picosecond pulse of spin-polarized electrons is launched, superdiffusing toward the FM/NM interface.

2. **Spin-to-Charge Conversion:** As this spin current is injected into the heavy NM layer (which possesses strong spin-orbit coupling), the Inverse Spin Hall Effect (ISHE) forces the electrons to deflect in opposite directions depending on their spin. This converts the longitudinal spin current into a transverse transient charge current, which ultimately radiates a broadband THz electromagnetic pulse into the far-field.

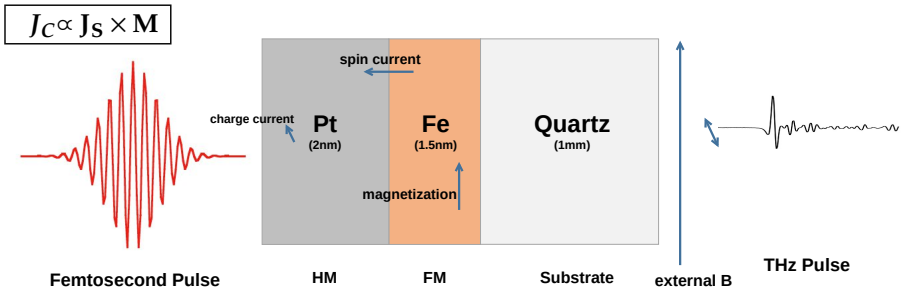

Figure 1.1: Schematic of a spintronic Fe/Pt THz emitter. A femtosecond laser pulse excites the Fe layer, driving a spin-polarized current (J_s) into the adjacent Pt layer. Due to the Inverse Spin Hall Effect, this is converted into a transverse charge current (J_c), generating a broadband THz pulse. (Adapted from Mag-usara et al. [5] and Wu et al. [4]).

The efficiency of this entire process is heavily dictated by the specific spin-dependent transport properties at the FM/NM interface. For an optimized Fe/Pt spintronic bilayer, Mag-usara et al. recently demonstrated that the Fe/Pt interface acts as an intrinsic spin filter, governed by the local density of states (LDOS) of the Fe d-orbitals [5]. Iron's electronic configuration is [Ar] $4s^2 3d^6$. When analyzing the spin-dependent transport at this interface, two distinct regimes emerge:

- **Spin-Up States:** Above a threshold of $\sim$0.25 eV relative to the Fermi level (E_f), the highly localized spin-up $3d$-states abruptly drop off. Consequently, the excited spin-up electrons propagate freely across the interface as highly mobile, delocalized $4s$ electrons.
- **Spin-Down States:** Conversely, the spin-down electronic structure exhibits a massive density of unoccupied $3d$-states high above E_f. These dense $3d$-states act as available traps, causing the spin-down electrons to undergo severe scattering and become trapped at the interface.

Because the highly mobile spin-up carriers easily transmit into the Pt while the spin-down carriers are trapped, the Fe/Pt interface creates a massive intrinsic spin-filter effect [5]. This filtering is directly responsible for maximizing the net spin polarization of the injected current, making Fe/Pt an exceptionally robust and efficient THz emitter.

1.3 Electronic Band Structures and Spin-Dependent Transport

To understand the macroscopic phenomena of ultrafast demagnetization and terahertz (THz) emission, it is essential to examine the microscopic electronic properties of the materials involved. The electronic band structure dictates the available density of states (DOS) at the

Fermi level (E_F), which in turn governs how hot electrons are excited by a femtosecond laser pulse, how quickly they thermalize, and how they transport through a heterostructure.

1.3.1 Nickel: fundamental model

Nickel (Ni) has long served as the fundamental model system for studying ultrafast spin dynamics. Its band structure is characterized by partially filled $3d$ bands that strongly overlap with broader, delocalized $4s$ bands right at the Fermi level.

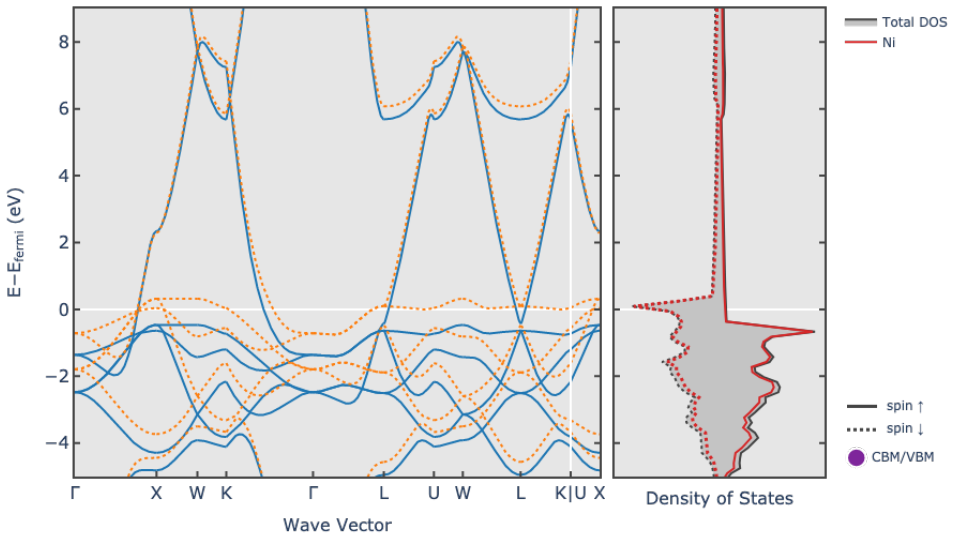

Figure 1.2: Electronic band structure of Nickel (Ni). The dense clustering of bands near the Fermi level (0 eV) facilitates rapid scattering. Image obtained from the Materials Project [6], licensed under CC BY 4.0.

Because of this high density of available d-states near E_F, optically excited non-thermal electrons in Nickel undergo rapid electron-electron and electron-phonon scattering. This allows pure Nickel to behave largely as a closed, local thermodynamic system. The energy remains confined within the film, driving local spin-flip scattering events that lead to complete demagnetization within tens to hundreds of femtoseconds, as famously described by early multi-temperature models [7].

1.3.2 Platinum: Heavy-Metal Spin-Sink

In contrast to ferromagnetic Nickel, Platinum (Pt) is a non-magnetic heavy metal with a very different electronic landscape. Its band structure is dominated by wide $5d$ bands and massive intrinsic spin-orbit coupling (SOC).

In spintronic THz emitters, Platinum acts as the ultimate "spin-sink". When a highly energetic population of non-thermal electrons is injected into Pt, they must find available states above the Fermi level to scatter into. At high laser fluences, these available states can fill up, leading to Pauli blocking. This forces the non-thermal electrons to survive longer before establishing a Fermi-Dirac temperature (τ_N), creating a thermodynamic bottleneck [9]. Once these electrons scatter, Pt's massive SOC efficiently converts the injected spin-polarized current into a transverse charge current via the Inverse Spin Hall Effect (ISHE), generating a THz pulse.

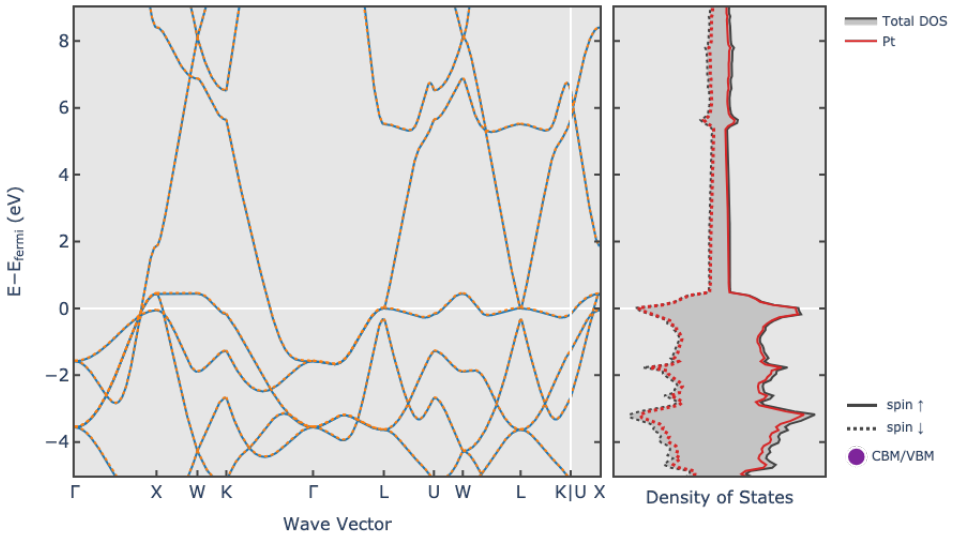

Figure 1.3: Electronic band structure of Platinum (Pt). The wide $5d$ bands provide available phase space for incoming hot electrons. Image obtained from the Materials Project [8], licensed under CC BY 4.0.

1.3.3 Iron: Spin-Polarized Injector

Iron (Fe) introduces the critical element of exchange splitting. Its band structure exhibits a distinct asymmetry between spin-up (majority) and spin-down (minority) bands.

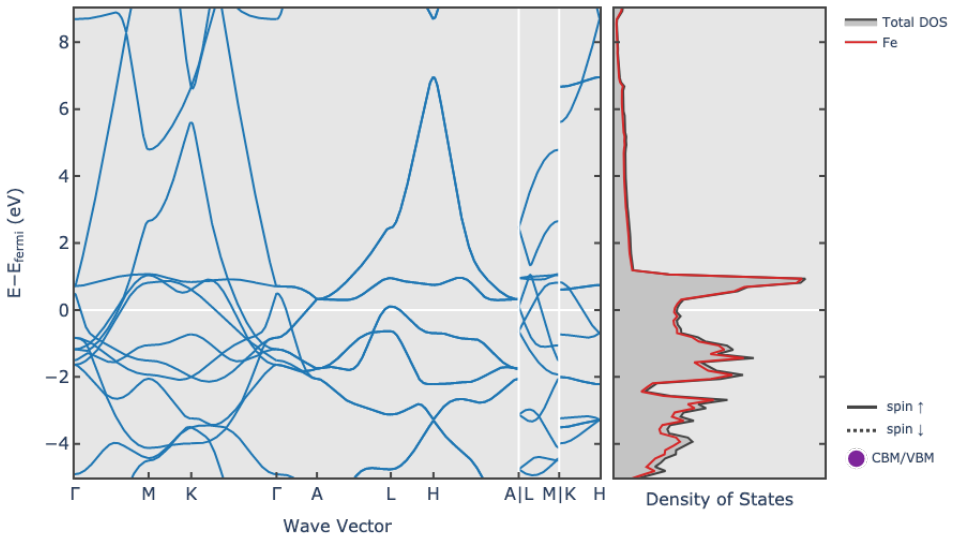

Figure 1.4: Electronic band structure of Iron (Fe). The exchange splitting between spin-up and spin-down configurations creates a natural spin filter at interfaces. Image obtained from the Materials Project [10], licensed under CC BY 4.0.

When a femtosecond laser excites the Fe layer, it creates a massive population of non-thermal hot electrons. Because the highly localized spin-up $3d$-states drop off rapidly just above E_F, excited spin-up electrons transition into highly mobile $4s$ states. Conversely, the spin-down electronic structure contains a massive density of unoccupied $3d$-states high above E_F, which act as traps. This means the Fe/Pt interface acts as an intrinsic spin filter: the mobile spin-up

carriers easily undergo superdiffusive transport into the Platinum layer, while the spin-down carriers scatter and remain trapped in the Iron [11].

Ultimately, combining these distinct electronic structures, namely the spin-filtering exchange splitting of Fe and the high-SOC phase space of Pt, creates the non-local superdiffusive transport that drives highly efficient spintronic THz emitters.

1.4 Motivation and Research Objectives

The development of highly efficient spintronic THz emitters requires a profound understanding of the fundamental energy dissipation limits in magnetic transition metals. While it is known that the interplay of structural birefringence, hot-electron diffusion, and spin-flip scattering [3] governs the macroscopic optical and terahertz responses, the exact microscopic energy flow often remains ambiguous. Resolving how varying laser excitation strengths perturb the delicate balance between the electronic, structural, and magnetic subsystems is critical to engineering the next generation of ultrafast spintronic devices.

Therefore, the primary objective of this research is to systematically investigate the ultrafast dynamics in Fe/Pt spintronic heterostructures and pure Nickel thin films as a function of incident laser fluence. By decoupling the transient reflectivity ($\Delta R/R$), we aim to quantitatively extract the temporal evolution of the various relaxation timescales which will allow us to accurately map the energy transfer rates among the spin lattice and thermal and non-thermal electron subsystems, ultimately identifying the physical bottlenecks that govern ultrafast demagnetization and optimal THz emission in these materials.

Chapter 2

Experimental Setup

Probing ultrafast carrier dynamics demands a precisely orchestrated optical architecture capable of synthesizing, amplifying, and characterizing phase-locked wave packets. This experimental framework relies on the intricate balance of nonlinear optical phenomena and stringent thermodynamic control. The following sections detail the generation of femtosecond pulses using a mode-locked Ti:Sapphire oscillator, the subsequent chirped pulse amplification chain, optical autocorrelation techniques, and the cryogenic and modulation parameters requisite for high fidelity lock-in detection.

2.1 Femtosecond Laser Oscillator: Coherent Mantis

This section is mainly based on the Mantis Laser Operator's Manual [12]

The foundation of our ultrafast spectrometer is the Coherent Mantis, a Ti:Sapphire oscillator engineered to sustain stable passive modelocking. Traditional continuous wave (CW) lasing relies strictly on frequency domain competition, where a gain medium selectively amplifies a narrow spectral band governed by its emission cross section and the cavity resonance conditions. The Ti:Sapphire crystal, however, exhibits immense homogeneous broadening driven by strong vibronic coupling within the crystal lattice [1]. This unique property yields an exceptionally broad gain bandwidth capable of supporting a vast manifold of longitudinal modes simultaneously, a strict prerequisite for the synthesis of ultrashort pulses [13].

2.1.1 Cavity Architecture and Optical Pumping

The macroscopic geometry of the Mantis cavity is folded to achieve strict spatial overlap between the external pump beam and the circulating intracavity infrared field. This extended path length dictates the fundamental repetition rate of the oscillator, locked near 80 MHz by the cavity round trip time [12].

Population inversion within the Ti:Sapphire crystal requires continuous excitation from a high intensity source. This is provided by an Optically Pumped Semiconductor Laser (OPSL). Distinct from conventional solid state crystals, the OPSL relies on epitaxially grown semiconductor quantum wells [14]. The fundamental emission wavelength is defined by the quantum confinement of charge carriers within these heterostructures. Approximating the confinement potential as a discrete one dimensional system, the quantized energy levels E_n for electrons and holes are dictated by [14]:

$$E_n = \frac{\hbar^2 n^2 \pi^2}{2m^* L^2} \tag{2.1}$$

where $\hbar$ is the reduced Planck constant, m^* is the effective carrier mass, and L represents the physical thickness of the quantum well layer. The energy of the emitted photon resulting from

electron-hole recombination is the sum of the bulk bandgap E_g and the ground state confinement energies of the electron (E_{e1}) and hole (E_{h1}):

$$E_{emission} = E_g + E_{e1} + E_{h1} \tag{2.2}$$

By precisely tailoring the quantum well thickness during epitaxial growth, a process known as bandgap engineering, the OPSL is strictly constrained to emit the exact fundamental infrared wavelength required [14].

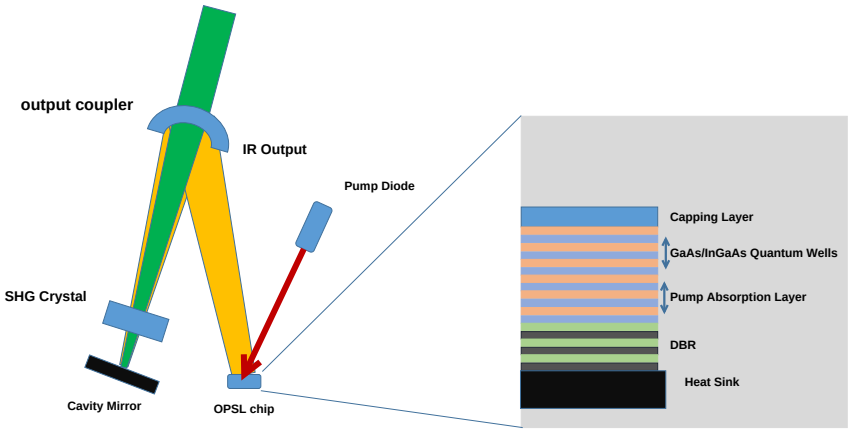

Figure 2.1: Cross-sectional view of the OPSL gain chip depicting the Distributed Bragg Reflector (DBR) and the active quantum well layers engineered for tailored emission. (Adapted from: [15])

To match the primary absorption peak of Ti:Sapphire, this fundamental beam undergoes intra-cavity Second Harmonic Generation (SHG) to produce a 532 nm pump field. The conversion efficiency of this process scales nonlinearly with the fundamental intensity, governed by the phase matching relation [16]:

$$P_{2\omega} \propto P_{\omega}^2 \cos^2\left(\frac{\Delta k L_{SHG}}{2}\right) \tag{2.3}$$

where P_ω is the fundamental power, Δk is the phase mismatch vector, and L_{SHG} is the interaction length of the nonlinear crystal.

2.1.2 Kerr-Lens Modelocking Dynamics

Transforming continuous emission into a coherent ultrashort pulse requires a phase relationship across all oscillating longitudinal modes. When locked in phase, these modes interfere constructively at a localized spatial coordinate, forming an intense singular wave packet that propagates through the cavity. The Mantis achieves this coherence passively utilizing the optical Kerr effect [12, 13]. The Ti:Sapphire crystal functions as an intensity dependent nonlinear medium where the total refractive index scales with the instantaneous optical intensity:

$$n(I) = n_0 + n_2 I(r,t) \tag{2.4}$$

Because the circulating beam assumes a Gaussian spatial profile, the on-axis intensity drastically exceeds the peripheral intensity. This localized gradient induces a higher refractive index at the beam center, establishing an instantaneous gradient index lens. This Kerr lensing effect drives a spatial collapse of the high intensity pulsed mode [12, 13].

By designing the cavity such that this tightly focused pulse exhibits maximum spatial overlap with the tightly focused pump beam inside the crystal, a mechanism of soft aperturing is established [12]. The focused pulse extracts gain exponentially faster than the diffuse CW mode, inherently forcing the cavity to favor the high peak power, modelocked state.

Because Kerr lensing relies on third order nonlinear susceptibility, it imposes a distinct intensity threshold. The cavity cannot spontaneously transition from a low intensity CW state into the modelocked regime. Passive modelocking must be externally initiated by introducing a transient boundary condition perturbation. Actuating the physical starter mirror (M7) introduces a rapid mechanical impulse to the cavity, generating an instantaneous noise spike in the field intensity [12]. This localized spike is sufficient to breach the nonlinear threshold, triggering the spatial collapse and locking the phases into a self sustaining state.

2.1.3 Dispersion Management and Soliton Equilibrium

Femtosecond pulses are inherently broadband wave packets. Propagation through any dielectric medium introduces chromatic dispersion. Expanding the propagation constant $k(\omega)$ in a Taylor series around the carrier frequency ω_0 reveals the impact of this dispersion [17]:

$$k(\omega) = k(\omega_0) + \left.\frac{\partial k}{\partial \omega}\right|_{\omega_0} (\omega - \omega_0) + \frac{1}{2}\left.\frac{\partial^2 k}{\partial \omega^2}\right|_{\omega_0} (\omega - \omega_0)^2 + \dots \tag{2.5}$$

The first order derivative defines the inverse group velocity, reflecting the bulk temporal transit. The critical parameter is the second order derivative, known as Group Velocity Dispersion (GVD) [17]. Normal dispersion within the sapphire lattice ($k'' > 0$) causes the lower frequency red components to outpace the higher frequency blue components. This effect linearly chirps the pulse, symmetrically stretching it in the time domain and fatally diluting the peak intensity required to sustain the saturable absorption of the Kerr lens.

To preserve the ultrashort temporal envelope, the cavity must be constrained to a net anomalous dispersion regime. This compensation is achieved using specialized chirped mirrors and a pair of intracavity fused silica wedges [12]. Translating these wedges modulates the exact propagation depth through the glass, allowing meticulous balancing of the net cavity phase. Concurrently, the extreme peak intensity drives Self Phase Modulation (SPM) within the crystal, a nonlinear parametric process that generates new spectral components and positively chirps the pulse. The dynamic equilibrium established between the anomalous GVD from the optics and the positive nonlinear phase shift from SPM governs the formation of a dissipative optical soliton [12]. The evolution of this field envelope $A(z,t)$ is dictated by the Nonlinear Schrödinger Equation:

$$\frac{\partial A}{\partial z} + \frac{i}{2}\beta_2 \frac{\partial^2 A}{\partial t^2} = i\gamma |A|^2 A \tag{2.6}$$

where β_2 represents the net cavity GVD and γ quantifies the SPM nonlinearity. A stable mode-locked pulse is fundamentally a manifestation of this exact physical balance.

2.2 Regenerative Amplification: Verdi V12 and RegA 9050

The pulses from the Mantis oscillator require amplification to drive nonlinear interactions in solid-state samples. The Coherent RegA 9050 amplifies these pulses using Chirped Pulse Amplification (CPA), pumped by a Coherent Verdi V12 laser delivering 12 W of continuous-wave 532 nm radiation [18–20]. The Verdi V12 utilizes a Neodymium-doped Yttrium Orthovanadate (Nd:YVO_4) crystal lasing at 1064 nm. Intracavity frequency doubling via a temperature-stabilized Lithium Triborate (LBO) crystal at 148°C generates the 532 nm output required for Ti:Sapphire pumping [19].

The RegA operates through the following sequence: First, the seed pulse from the Mantis is temporally stretched to picosecond duration via a positive chirp, reducing peak intensity to prevent optical damage during amplification [18, 20]. This stretched pulse enters the Ti:Sapphire cavity through a Faraday Isolator. An Acousto-Optic Q-switch, normally held in high-loss state to suppress continuous-wave lasing, briefly switches to low-loss mode, allowing the seed pulse to make multiple cavity round trips while extracting stored energy from the continuously pumped gain medium [18]. The amplified pulse is then ejected via the Cavity Dumper and routed through a grating compressor, which applies negative group velocity dispersion to recompress the pulse to femtosecond duration.

2.3 Integrated Setup Architecture

The complete system links the oscillator, amplification chain, and diagnostics into a phase-locked beamline. This configuration produces a stable 250 kHz pulse train, providing the temporal resolution required to capture ultrafast carrier dynamics and phonon dynamics in the samples studied in this thesis. This whole process requires the pulsed laser to be generated in the Mantis, passed on to stretcher, where the stretched pulse is amplified by RegA 9050, which is pumped by Verdi. The laser is then routed to compressor, after which they are ready for use in experiments. This whole procedure produces output with:

- Repetition rate: 250 kHz (reduced from the original 80 MHz)
- Average output power: ∼1.2 W (1.6W after RegA)
- Pulse energy: ∼4.8 μJ per pulse
- Pulse duration after compression: ∼70 fs

2.4 Pulse Characterization: Delta Autocorrelator

Direct electronic measurement of femtosecond transients is prohibited by the inherent bandwidth limitations and capacitance of conventional photodiodes. Pulse characterization must therefore rely on nonlinear optical gating techniques. We utilize a Delta Single Shot Autocorrelator manufactured by Minioptic Technology, Inc. to determine our absolute temporal resolution [21].

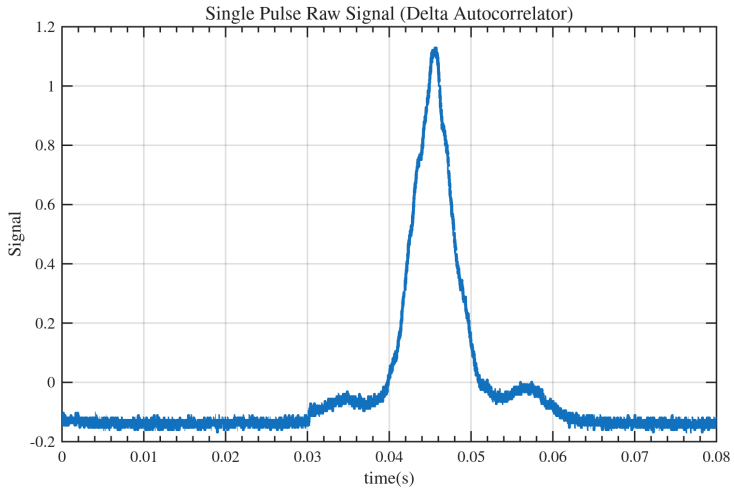

Figure 2.2: A single shot autocorrelation spatial trace, serving as the raw data for extracting the temporal full width at half maximum of the amplified pulse.

The correlator exploits background free intensity autocorrelation via non-collinear Second Harmonic Generation [21]. The input pulse is divided into two identical replicas by a beam splitter. These replicas are directed into a Beta Barium Borate crystal such that their propagation vectors intersect at a finite crossing angle. Due to momentum conservation, the second harmonic field is generated exclusively along the spatial bisector of the two beams, and only exists where the two optical wave packets overlap simultaneously in both space and time. This specific geometric crossing angle uniquely maps the relative temporal delay τ onto a transverse spatial coordinate x across the crystal plane [21]. A CCD sensor captures the spatial intensity profile of this second harmonic emission. The measured integrated intensity $I_c(\tau)$ represents the convolution of the pulse with itself:

$$I_c(\tau) \propto \int_{-\infty}^{\infty} I(t)I(t-\tau)\,dt \tag{2.7}$$

Converting this spatial profile into an absolute temporal duration requires rigorous calibration of the time-to-space axis. Calibration is achieved by translating the internal optical delay stage by a precise microscopic distance Δd. Because the optical pulse traverses this delay line twice, the induced temporal delay $\Delta\tau$ is determined by:

$$\Delta\tau = \frac{2\Delta d}{c} \tag{2.8}$$

where c is the speed of light. In our protocol, inducing a translation of $\Delta d = 0.05$ mm generates a known optical delay of approximately 333.3 fs. We observe that this physical translation shifts the centroid of the autocorrelation trace by exactly 11.7 ms on our oscilloscope timebase. This yields a direct calibration factor $\mathcal{C}$ linking the oscilloscope readout to the true optical delay:

$$\mathcal{C} = \frac{2\Delta d/c}{\Delta t_{shift}} = \frac{333.3 \text{ fs}}{11.7 \text{ ms}} \approx 28.49 \text{ fs/ms} \tag{2.9}$$

The experimental autocorrelation trace produced a full width at half maximum (Δt_{FWHM}) of 4.0ms. Assuming a standard sech^2 pulse envelope, the true pulse duration τ_p is deconvolved from the autocorrelation width by dividing by the geometric shape factor of 1.543 [21]:

$$\tau_p = \frac{\Delta t_{FWHM} \times \mathcal{C}}{1.543} \tag{2.10}$$

Applying this specific relation to our measured 4.0ms FWHM fit yields an ultimate compressed pulse width of 72.51 fs. This diagnostic confirms that the grating compressor is rigorously optimized. Alternatively, one can follow the formalism stated in the Delta Autocorrelator Operator Manual [21], to get the same result.

2.5 PID Control

Temperature stabilization was achieved using a Cryo-con Model 32 controller coupled to a Janis VNF-100 liquid nitrogen cryostat [22]. The system employs PID (Proportional-Integral-Derivative) feedback control to maintain the sample at the desired temperature with stability better than ± 0.1 K. The PID parameters were optimized using the Ziegler-Nichols closed-loop tuning method [22]. Critical oscillation measurements at 95 K yielded an ultimate gain $K_u = 150$ and ultimate period $T_u = 6.8$ s. Following standard tuning formulas [22], the controller was configured with $P = 60$, $I = 5.44$, and $D = 0.5$ for stable operation across the measurement range (77–300 K). Heater ranges were automatically interpolated, with mid-range heating below 85 K and high-range above 85 K to optimize thermal response. Temperature monitoring and data acquisition were performed via GPIB interface using a custom Python script, enabling automated measurements with real-time logging of sample temperature during optical pump-probe and Terahertz TDS experiments. Detailed SOP can be found in Appendix A.

2.6 Acousto-Optic Modulation and Phase Matching

Isolating minute photoinduced transient dynamics from the overwhelming equilibrium background necessitates high frequency lock-in amplification. This requires the optical pump beam to be periodically modulated. We can improve this modulation more than chopper, by utilizing an acousto-optic modulator (AOM).

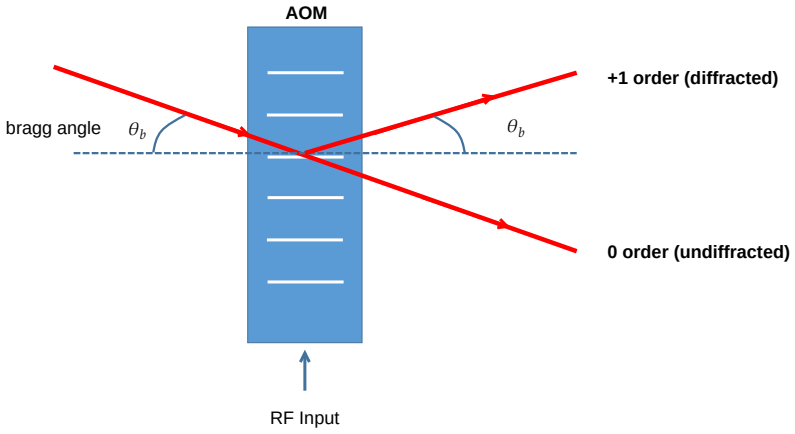

Figure 2.3: Top-down perspective of the AOM diffraction geometry, isolating the modulated first order beam from the un-diffracted zero order transmission.

The AOM exploits the photoelastic effect [17]. A piezoelectric transducer bonded to the crystal is driven by a radio frequency signal generator. The transducer injects acoustic phonons into the lattice, creating propagating regions of alternating high and low density. This acoustic wave modulates the local refractive index, establishing a dynamic, volumetric diffraction grating traveling at the speed of sound through the medium [17]. When the incident laser intersects this acoustic grating, a fraction of the optical power is diffracted. Because the amplitude of this diffracted field is directly coupled to the applied RF power, toggling the RF signal inherently chops the optical beam at the desired reference frequency.

Maximum energy transfer into the first order diffracted beam demands strict adherence to the Bragg condition [17]. The interaction between the incident photon (wavevector $\vec{k}_{inc}$) and the acoustic phonon (wavevector $\vec{K}$) must rigorously conserve momentum:

$$\vec{k}_{diff} = \vec{k}_{inc} \pm \vec{K} \tag{2.11}$$

This phase matching constraint dictates that the crystal must be oriented such that the incident light strikes the acoustic wavefronts at the specific Bragg angle θ_b, given by:

$$\sin(\theta_b) = \frac{\lambda}{2\Lambda} \tag{2.12}$$

where λ represents the optical wavelength and Λ is the acoustic wavelength within the material [17]. By mounting the AOM on a high precision rotation stage and continuously tuning the incidence angle to satisfy this momentum conservation requirement, we successfully confirmed an 85% diffraction efficiency. This metric ensures that the vast majority of the optical pump power is transferred into the modulated beam directed toward the sample, optimizing the ultimate signal to noise ratio of the lock-in detection scheme.

Chapter 3

Ultrafast Pump-Probe Spectroscopy

3.1 Introduction to Time-Resolved Spectroscopy

The macroscopic physical properties of condensed matter are inherently dictated by the microscopic, dynamic interactions between its fundamental constituents: charge carriers, lattice vibrations (phonons), and spins [1]. These fundamental scattering events occur on phenomenally short timescales. For instance, electron-electron thermalization typically unfolds within tens to hundreds of femtoseconds, while electron-phonon coupling and the subsequent thermalization with the lattice lattice generally occur on the timescale of 1 to 10 picoseconds [1, 23]. Spin-lattice relaxation and acoustic phonon propagation extend into the hundreds of picoseconds.

Conventional continuous-wave (CW) optical spectroscopy acts as a slow integrator. It averages over all these rapid dynamic processes, completely obscuring the transient, highly non-equilibrium states that govern phase transitions, energy transfer, and material functionality [23]. To arrest these dynamics and observe them in real time, we must employ ultrafast pump-probe spectroscopy [1]. The core philosophy of this technique involves pushing the system violently out of thermal equilibrium using an intense femtosecond laser pulse, known as the pump. This excitation injects energy into the electronic subsystem, creating a highly non-thermal, excited carrier distribution that deviates wildly from the standard Fermi-Dirac statistics governing equilibrium states [1]. As these hot carriers scatter and transfer their energy to the lattice and spin systems, the complex dielectric function of the material, $\tilde{\epsilon}(\omega)$, dynamically evolves.

3.1.1 Mapping Observables to Transient Electrodynamics

To understand this state, a secondary, much weaker pulse, the probe, is directed at the sample after a precisely controlled temporal delay, τ. The interaction of this probe with the material is governed fundamentally by the transient complex index of refraction, $\tilde{n}(\omega, \tau) = n(\omega, \tau) + i\kappa(\omega, \tau)$, which is directly tied to the complex dielectric function [1]. The pump excitation essentially induces a time-dependent perturbation $\Delta\tilde{n}(\omega, \tau)$ upon the equilibrium state.

Experimentally, we cannot directly measure $\tilde{n}$; we only have access to macroscopic observables, specifically the reflected intensity R and transmitted intensity T. For a bulk material probed at near-normal incidence, the equilibrium reflectivity is derived from the Fresnel equations [1, 24]:

$$R(\omega) = \left|\frac{\tilde{n}(\omega) - 1}{\tilde{n}(\omega) + 1}\right|^2 = \frac{(n-1)^2 + \kappa^2}{(n+1)^2 + \kappa^2} \tag{3.1}$$

In a pump-probe experiment, the lock-in amplifier detects the minuscule differential change in the probe's reflection, $\Delta R(\tau)$, normalized to the static reflection, R. Using first-principles electrodynamics, we can map this measured fractional change to the underlying physical changes

in the complex index of refraction via a first-order Taylor expansion [1]:

$$\frac{\Delta R(\tau)}{R} = \frac{\partial \ln R}{\partial n}\Delta n(\tau) + \frac{\partial \ln R}{\partial \kappa}\Delta \kappa(\tau) \tag{3.2}$$

This relationship explicitly demonstrates that our transient optical signal is a weighted linear combination of the dispersive (Δn) and absorptive ($\Delta \kappa$) perturbations induced by the pump. It is crucial to note that these two components are not independent; they are rigidly linked through the Kramers-Kronig relations, meaning a change in the absorption spectrum will necessarily induce a broad spectral change in the refractive index [1, 24].

For thin-film samples, transmission measurements provide a complementary mapping. The transmission T relates heavily to the optical absorption coefficient $\alpha(\omega) = 2\omega\kappa(\omega)/c$. The fractional change in transmission, $\Delta T/T$, under the assumption of small perturbations and neglecting multiple-reflection Fabry-Pérot interference fringes, is exponentially dependent on the transient change in the absorption coefficient $\Delta\alpha(\tau)$ integrated over the effective penetration depth or film thickness d:

$$\frac{\Delta T(\tau)}{T} \approx -\Delta\alpha(\tau)d \tag{3.3}$$

By tracking these macroscopic proxies ($\Delta R/R$ and $\Delta T/T$) as a function of the delay time τ, one can even effectively reconstruct the temporal evolution of the material's carrier pathways. The ultimate temporal resolution of this mapping is strictly limited by the cross-correlation of the pump and probe pulse widths, defining the instrumental response function of the setup, rather than the bandwidth of any electronic detector [1].

3.2 Experimental Architecture

The standard topology of our pump-probe setup partitions the fundamental 800 nm output of the Ti:Sapphire oscillator (such as the Mantis system) into two distinct paths. The more intense portion is directed into the pump line to induce the primary excitation, while the weaker fraction is steered into the probe line to monitor the subsequent relaxation dynamics.

3.3 Second Harmonic Generation for a 400 nm Pump

To achieve a versatile two-color pump-probe configuration and drastically improve signal-to-noise isolation, the 800 nm fundamental pump beam is frequency-doubled to 400 nm using a Beta Barium Borate (BBO) nonlinear optical crystal.

3.3.1 Physical Origin of Nonlinear Polarization

In classical, linear optics, the electron clouds of a dielectric medium act as harmonic oscillators. When an external electric field $E(t)$ is applied, the induced dipole polarization $P(t)$ responds linearly: $P(t) = \epsilon_0\chi^{(1)}E(t)$, where $\chi^{(1)}$ is the linear susceptibility [16]. However, under the extreme electric field intensities associated with femtosecond laser pulses, the restoring force of the atomic potential is no longer perfectly harmonic. The electron cloud is driven so far from its equilibrium position that it samples the anharmonic regions of the binding potential. Consequently, the induced polarization must be expanded as a Taylor series in terms of the applied electric field [16]:

$$P(t) = \epsilon_0\left(\chi^{(1)}E(t) + \chi^{(2)}E^2(t) + \chi^{(3)}E^3(t) + \dots\right) \tag{3.4}$$

Second Harmonic Generation (SHG) arises explicitly from the second-order term, $P^{(2)}(t) = \epsilon_0\chi^{(2)}E^2(t)$. Consider an incident fundamental optical wave oscillating at a carrier frequency

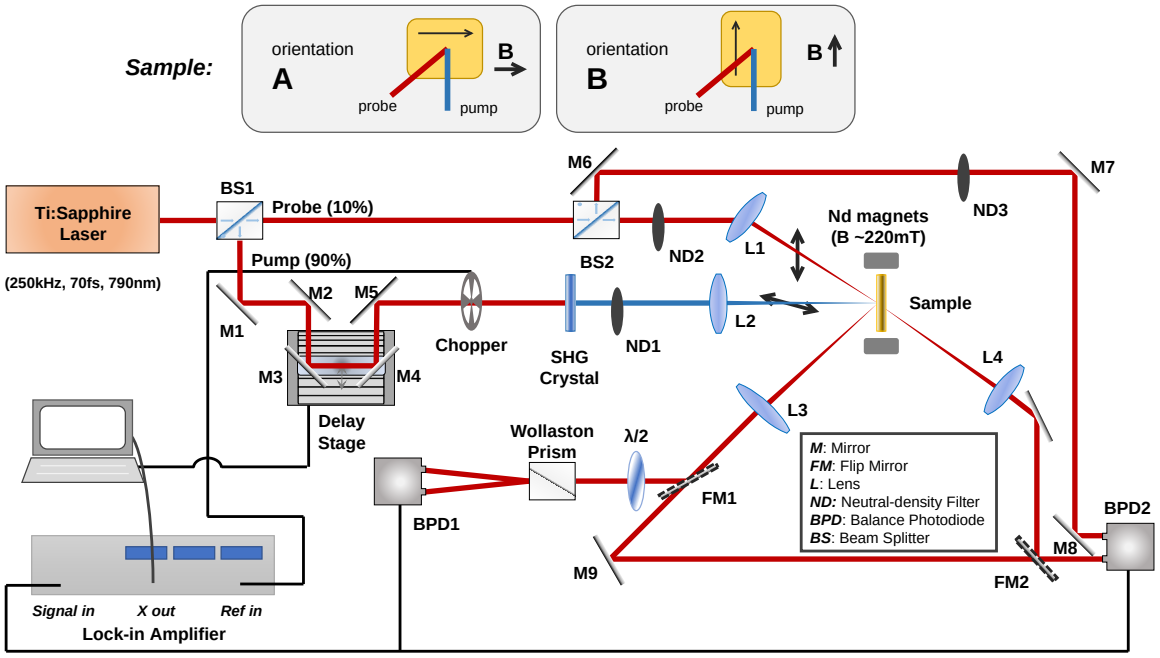

Figure 3.1: Detailed schematic diagram of the two-color pump-probe setup. The fundamental 800 nm light is split into a pump and probe arm. The pump passes through a BBO crystal for second harmonic generation to 400 nm, an optical chopper for modulation, and a mechanical delay stage to control the temporal offset. The probe reflects off the sample and is analyzed by a balanced detection system which goes to lockin amplifier via current amplifier.

ω, described by $E(t) = E_0 \cos(\omega t)$. Substituting this into the second-order polarization term yields:

$$P^{(2)}(t) = \epsilon_0 \chi^{(2)} E_0^2 \cos^2(\omega t) \tag{3.5}$$

By applying the trigonometric power-reduction identity, $\cos^2(\theta) = \frac{1}{2}(1 + \cos(2\theta))$, we can rewrite the nonlinear polarization as [16]:

$$P^{(2)}(t) = \frac{1}{2}\epsilon_0 \chi^{(2)} E_0^2 + \frac{1}{2}\epsilon_0 \chi^{(2)} E_0^2 \cos(2\omega t) \tag{3.6}$$

This expansion is profoundly revealing. The first term is a static (DC) electric field, a phenomenon known as optical rectification. The second term, crucially, represents a localized dipole oscillating at exactly twice the driving frequency (2ω). According to classical electrodynamics, an oscillating dipole radiates an electromagnetic wave at its oscillation frequency. Thus, the material physically radiates a new photon field at 400 nm, effectively annihilating two 800 nm photons to create a single 400 nm photon [16].

3.3.2 The Requirement for Non-Centrosymmetric Crystals

It is a strict physical requirement that SHG can only occur in materials lacking inversion symmetry (non-centrosymmetric crystals) [16]. We can prove this by examining the spatial symmetry of the polarization. If a material possesses inversion symmetry, flipping the direction of the applied electric field (from E to $-E$) must result in an exactly equal but opposite polarization response (from P to $-P$). Mathematically, $P(-E) = -P(E)$.

Now, let us test the second-order polarization term under this symmetry condition:

$$P^{(2)}(-E) = \epsilon_0 \chi^{(2)} (-E)^2 = \epsilon_0 \chi^{(2)} E^2 = P^{(2)}(E) \tag{3.7}$$

This shows that $P^{(2)}(-E) = P^{(2)}(E)$. However, the fundamental rule of the centrosymmetric lattice dictates $P(-E) = -P(E)$. The only way both conditions can be true simultaneously is if $P^{(2)} = -P^{(2)}$, which requires that $P^{(2)} = 0$. Therefore, the second-order nonlinear susceptibility tensor $\chi^{(2)}$ must be identically zero in any material with a center of inversion [16]. This is precisely why specialized, asymmetric crystals like BBO are required to physically rotate the polarization non-linearly and generate the 2ω field.

3.3.3 Phase Matching and Birefringence

Generating the 400 nm radiation is only half the battle; ensuring that the generated waves constructively interfere as they propagate through the bulk of the crystal is equally critical. For efficient energy transfer from the fundamental to the second harmonic, the phase velocities of the two interacting waves must be identical. This condition is known as phase matching and represents the conservation of momentum for the interacting photons [16]:

$$\Delta k = k(2\omega) - 2k(\omega) = 0 \tag{3.8}$$

Because the wavevector is defined as $k = n(\omega)\omega/c$, the condition $\Delta k = 0$ implies that the refractive index must be exactly the same for both frequencies: $n(2\omega) = n(\omega)$. In any normal dispersive material, the refractive index increases with frequency, meaning the blue light (400 nm) will always travel slower than the red light (800 nm). Because $n(2\omega) > n(\omega)$, the generated 400 nm waves from different depths within the crystal will drift out of phase and destructively interfere, resulting in an oscillating, low-intensity output known as Maker fringes [16].

To circumvent normal dispersion, we exploit the physical property of birefringence found in anisotropic crystals. BBO has two distinct refractive indices depending on the polarization of light relative to the crystal's optical axis: an ordinary index (n_o) and an extraordinary index (n_e) [16]. In Type-I phase matching, we inject the 800 nm light polarized along the ordinary axis. The crystal is then physically rotated to a specific tuning angle θ such that the extraordinary refractive index for the 400 nm light exactly matches the ordinary refractive index for the 800 nm light:

$$n_e(2\omega, \theta) = n_o(\omega) \tag{3.9}$$

By finding this precise phase-matching angle, the Δk mismatch is driven to zero, allowing the 2ω intensity to build up quadratically over the length of the crystal. Beyond extending our spectral reach, utilizing a 400 nm pump provides a massive experimental advantage in signal isolation [1]. Because the lock-in detector is searching for miniscule changes in the weak 800 nm probe, any scattered pump light reaching the photodiode would create an overwhelming artifact. By pumping at 400 nm, we can insert a strict 800 nm narrow-bandpass filter directly in front of the detector, optically rejecting all scattered pump photons before they can contaminate the signal.

3.4 Delay Stage and Phase-Sensitive Detection

The core variable in any time-resolved measurement is the time delay between the pump and the probe. Because we cannot electronically resolve femtosecond timescales, we map time onto physical distance [1]. This is achieved using a retroreflector mounted on a high-precision motorized linear translation stage in the pump optical path. Light travels at approximately 3×10^8 meters per second, meaning it takes about 3.3 picoseconds to traverse one millimeter. By moving the retroreflector a physical distance Δx, we alter the path length by $2\Delta x$, due to the light traveling to the mirror and back. The corresponding temporal delay Δt introduced is simply:

$$\Delta t = \frac{2\Delta x}{c} \tag{3.10}$$

A stage movement of just 1.5 micrometers introduces a temporal shift of 10 femtoseconds, highlighting the need for extreme mechanical stability.

The changes in the probe intensity induced by the pump are extraordinarily small, often on the order of one part in ten thousand to one part in a million. To extract such minuscule signals from the ambient electronic noise and laser fluctuations, we employ a lock-in amplifier coupled with an optical chopper [1]. The chopper is placed in the pump path, physically modulating the beam on and off at a specific reference frequency, f_{ref}. Consequently, the pump-induced changes in the sample only occur at this exact frequency. The lock-in amplifier takes the raw voltage output from the photodiode, which contains the tiny signal buried in noise, and multiplies it by a pure sine wave generated at f_{ref}. It then integrates this product over a defined time constant (acting as an extreme low-pass filter). Any noise component at a frequency different from the chopper frequency averages to zero, while the signal precisely at the chopper frequency yields a measurable DC voltage. This phase-sensitive detection suppresses $1/f$ noise and isolates the pure pump-induced response [1].

3.5 Beam Characterization and Fluence Calculation

Quantifying the exact energy deposited into the sample is mandatory for understanding the excitation density. This is characterized by the optical fluence, defined as the energy per unit area per pulse. The output of a well-aligned oscillator approximates a Gaussian spatial profile [17]. The intensity distribution as a function of radial distance r from the beam center is given by:

$$I(r) = I_0 \exp\left(\frac{-2r^2}{w^2}\right) \tag{3.11}$$

where w is the beam radius at which the intensity falls to $1/e^2$ of its peak value I_0. To measure w, we relay on **power through aperture**. Comparing the input and output power of the beam through a $50\mu m$ Aperture, one can directly map the gausian profile and calculate the beam diameter [17]. Calculating the power through aperture simultaneously for both pump and probe ensures that they are passing through and are focused at the same point. Once the beam radius w is known, the fluence Φ is calculated by taking the average power P_{avg} and the laser repetition rate f_{rep} to find the energy per pulse $E_{pulse} = P_{avg}/f_{rep}$. The fluence at the center of the Gaussian beam is then calculated as [1]:

$$\Phi = \frac{E_{pulse}}{\pi w^2} \tag{3.12}$$

In practice, the excitation geometry usually involves a pump spot size that is significantly larger than the probe spot size. This configuration ensures that the probe is reading out the dynamics from a region of spatially uniform carrier density at the center of the pump profile, avoiding artifacts that would arise if the probe sampled the cooler edges of the excitation volume [1].

3.6 Detection Modalities: Reflection and Transmission

Depending on the sample thickness and substrate transparency, measurements are taken in either a reflection or transmission geometry [1]. In a reflection geometry, the probe beam is focused onto the sample surface and the specular reflection is directed into the detector. The lock-in amplifier records the differential change in reflectivity, denoted as ΔR. We normalize this by the static reflectivity R (measured with the pump blocked) to yield the fractional change

$\Delta R/R$. This modality is highly sensitive to the surface properties and the penetration depth of the optical fields.

Conversely, in transmission geometry, the probe passes completely through the sample. The recorded signal is $\Delta T/T$. While reflection probes the surface boundary conditions heavily influenced by the complex refractive index changes, transmission integrates the absorption coefficient changes across the entire bulk of the sample volume. According to the fundamental principle of energy conservation in linear optics, the incident electromagnetic energy is strictly partitioned into reflected, transmitted, and absorbed fractions. This physical relationship is defined as [24]:

$$1 = R(\omega) + T(\omega) + A(\omega) \tag{3.13}$$

Consequently, tracking ΔR and ΔT allows for the complete reconstruction of the transient absorption dynamics ΔA. The physical interpretation of the carrier dynamics remains largely consistent across both modalities, though transmission avoids some of the complex interference effects seen in thin films on reflective substrates [1].

3.7 Anisotropic and Magneto-Optic Measurements

To investigate spin dynamics and magnetic ordering, the scalar measurement of raw intensity is insufficient. The polarization state of the light carries the critical information regarding the magnetization of the material [3]. When linearly polarized light reflects from a magnetic surface, the plane of polarization rotates, a phenomenon known as the Magneto-Optic Kerr Effect (MOKE). Our setup adapts the standard pump-probe scheme to measure this polarization rotation. We place a linear polarizer in the reflected probe path to clean the polarization state. This is followed by a Wollaston prism, a birefringent optical element that geometrically separates the beam into two orthogonal linear polarization components, generally termed s-polarization and p-polarization [1]. These two separated beams are routed into a balanced photodiode detector.

The Wollaston prism is initially rotated to a 45-degree angle relative to the incoming polarization when the sample is at equilibrium. At this precise angle, the intensity is split perfectly evenly between the two output channels, I_1 and I_2. The balanced detector hardware subtracts these two photocurrents, yielding a zero-voltage baseline ($I_1 - I_2 = 0$). When the pump pulse strikes the sample, it alters the magnetic state, causing a transient rotation of the probe's polarization by an angle $\Delta\theta$ [3]. This rotation unbalances the projection onto the Wollaston prism axes. One channel sees an increase in intensity while the other sees a proportional decrease. The differential signal measured by the lock-in amplifier becomes directly proportional to the rotation angle [3]:

$$\Delta I = I_1 - I_2 \propto \Delta\theta \tag{3.14}$$

It is crucial to recognize that this configuration operates as an incomplete MOKE measurement. In a strict MOKE setup, an external magnetic field is applied and modulated between $+B$ and $-B$. Measuring the difference isolates the pure magnetic signal from non-magnetic artifacts, allowing calculation of the absolute saturation magnetization M_0 [3]. Because our setup lacks an actively modulated magnetic field, we are simply taking a static measure of the transient change in the angle of the reflected probe. Pumping the sample deposits massive amounts of energy, creating thermal expansion, acoustic phonons, and changes in the optical index of refraction. These are isotropic thermal artifacts that also change the raw reflectivity. By using the balanced detection scheme, common-mode amplitude noise (where I_1 and I_2 both rise or fall together due to thermal changes in total reflectivity) is heavily suppressed through subtraction. However, the exact cancellation of all thermal and non-magnetic birefringent artifacts remains challenging without the explicit $+B$ and $-B$ field modulation. Although the

recorded signal is an accurate representation of the anisotropic response, it must be carefully interpreted to untangle the genuine spin dynamics from the coupled thermal background [3]. Hence, we have decided to not include the results for the same in this report.

Chapter 4

Ultrafast Carrier and Spin Dynamics in Metals

4.1 Principles of Pump-Probe Spectroscopy Across Material Classes

Time-resolved pump-probe spectroscopy is a powerful technique for investigating ultrafast carrier dynamics in solid-state materials [1]. The fundamental principle relies on using an ultrashort laser pulse (the pump) to trigger a highly energetic, non-equilibrium event, which is subsequently recorded in the time domain by a weaker, time-delayed optical pulse (the probe) [1]. The probe pulse measures the transient changes in the material's optical properties, typically taking the form of differential reflectivity ($\Delta R/R$) or differential transmission ($\Delta T/T$) [1].

The specific optical response and the underlying carrier dynamics depend fundamentally on the electronic band structure of the material under investigation, which defines the strict differences between insulators, semiconductors, and metals [1].

In semiconductors and insulators, the presence of a fundamental energy bandgap (E_G) strictly governs the optical excitation [1]. To excite carriers, the pump photon energy must exceed this threshold energy ($h\nu > E_G$) to promote an electron from the valence band into the conduction band, thereby creating an electron-hole pair [1]. Once these carriers are excited, the optical properties of the semiconductor are heavily influenced by state-filling (often referred to as Pauli blocking or bleaching) [1]. Because the newly occupied states in the conduction and valence bands block further absorption of probe photons, the interband absorption is proportionally reduced; this is mathematically represented by the reduction factor $(1 - f_e - f_h)$, where f_e and f_h are the distribution functions of the electrons and holes, respectively [1]. Additionally, the presence of these excited electron-hole pairs screens the Coulomb interactions within the lattice, leading to excitonic bleaching and a transient shrinkage of the bandgap known as bandgap renormalization [1].

Metals behave fundamentally differently due to the absence of a bandgap and the presence of a massive density of free conduction electrons [1]. Because there is no energy threshold near the Fermi level, *any* amount of photon energy is sufficient to excite the metallic system. The optical excitation in metals can occur via continuous intraband transitions (free-carrier absorption) or via interband transitions (e.g., from fully occupied, highly localized d-bands to unoccupied s, p-states above the Fermi level, E_F) [1]. In conventional optical reflectivity measurements, these interband transitions are often entirely masked by the dominant free-electron Drude response up to the plasma energy of the metal (which is typically between 4 to 10 eV) [1].

To bypass this masking and probe the actual carrier dynamics in metals, pump-probe spectroscopy exploits femtosecond thermomodulation [1]. When the intense pump pulse strikes the metal, it rapidly heats the electron bath and transiently broadens (smears) the Fermi-Dirac dis-

tribution [1]. This Fermi-level smearing suddenly opens previously blocked states below E_F and blocks previously available states above E_F for optical transitions [1]. As a result, the probe pulse detects a sharp, derivative-like feature in the transient absorption spectrum exactly at the transition energy bridging the deep d-bands and the Fermi level [1]. This purely electronic bleaching effect serves as our primary optical window into the ultrafast dynamics of metals, allowing us to track exactly how fast the hot electrons cool and thermalize with the underlying lattice [1].

4.2 Microscopic Physics of the Optical Response in Metals

To understand the complex ultrafast dynamics encoded in pump-probe spectroscopy, it is essential to chronologically break down the physical events occurring within the metal during and immediately after the laser excitation. By precisely tracking the differential reflectivity ($\Delta R/R$) and differential transmission ($\Delta T/T$), we can map the transition from a highly non-equilibrium quantum state to a classical thermodynamic regime.

4.2.1 Negative Delay and Pulse Overlap ($t \leq 0$)

At negative time delays ($\Delta t < 0$), the weaker probe pulse arrives at the sample before the intense pump pulse. During this phase, the probe simply interrogates the unperturbed, ground-state electronic structure of the metal, establishing the baseline static reflectivity (R_0) and transmission (T_0) values [1].

At exactly zero delay ($\Delta t = 0$), the pump and probe pulses spatially and temporally overlap on the sample surface. For transition metals, the intense femtosecond pump pulse (typically operating in the near-infrared or visible spectrum, e.g., 1.55 eV or 3.1 eV) promotes electrons from deep, fully occupied states (such as localized $3d$-bands) into unoccupied states (such as highly mobile $4sp$-bands) above the Fermi level (E_F) [3]. This instantaneous optical excitation generates a highly energetic, non-thermal electron distribution that strictly deviates from the standard Fermi-Dirac statistics [3].

4.2.2 State Filling and Dichroic Bleaching

Within the first few tens to hundreds of femtoseconds, these highly energetic non-thermal electrons undergo violent electron-electron (e-e) scattering [1]. This rapid scattering thermalizes the electron bath, establishing a defined, but extremely elevated, electron temperature (T_e). The macroscopic consequence of this drastic increase in T_e is the severe broadening, or 'smearing,' of the Fermi-Dirac occupation distribution around E_F [1].

This Fermi-level smearing is the primary mechanism that alters the metal's optical properties [1]. Because the previously empty electronic states just above E_F are now filled with hot electrons, and the previously occupied states just below E_F are now vacant (holes), the material's ability to absorb subsequent photons is fundamentally disrupted. When the delayed probe pulse arrives, it finds that the specific interband optical transitions it would normally drive are now Pauli-blocked. This pump-induced reduction in oscillator strength is referred to as the *state-filling effect* or *dichroic bleaching* [3].

4.2.3 Differential Transmission vs. Differential Reflectivity

The phenomenon of bleaching directly dictates the transient optical signals recorded by the photodetectors, but it manifests very differently in transmission versus reflection geometries.

If the material is sufficiently thin to allow transmission, the bleaching effect renders the sample transiently more transparent to the probe light [3]. For small optical perturbations, the

differential transmission ($\Delta T/T$) is directly proportional to the pump-induced change in the material's absorption coefficient ($\Delta\alpha$):

$$\frac{\Delta T}{T} \approx -\Delta\alpha d \tag{4.1}$$

where d is the sample thickness [25]. Because bleaching represents a drop in absorption ($\Delta\alpha < 0$), the differential transmission typically exhibits a positive peak upon laser excitation.

Conversely, the differential reflectivity ($\Delta R/R$) presents a significantly more complex behavior. The reflection of the probe beam is governed by the Fresnel equations, which depend on both the real (ϵ_1) and imaginary (ϵ_2) parts of the metal's transient complex dielectric permittivity tensor, $\epsilon(T_e, T_l) = \epsilon_1 + i\epsilon_2$ [26]. As the electron and lattice temperatures (T_e and T_l) evolve, they dynamically alter both components of ϵ. Because the Fresnel equations map these dielectric changes non-linearly to the reflected intensity, a decrease in absorption (bleaching) does not simply equate to a uniform increase or decrease in reflectivity.

Instead, the sign and magnitude of the $\Delta R/R$ signal are highly sensitive to the specific wavelength of the probe pulse relative to the material's band structure [1, 25]. As demonstrated in experiments on various metals, probing at energies directly corresponding to the d-band to E_F transition yields a sharp, derivative-like spectral feature in the reflectivity signal [1]. Consequently, depending on the exact probe wavelength, the $\Delta R/R$ and $\Delta T/T$ signals can exhibit opposite polarities and distinctly different relaxation dynamics [25].

4.3 The Drude Model and the Scattering Rate (γ)

While the initial optical response near zero delay is governed by quantum state-filling and non-thermal bleaching, this highly energetic electron population is short-lived. Within approximately 100 femtoseconds, violent electron-electron scattering events thermalize the electron bath, establishing a well-defined electron temperature (T_e) [25]. Once the electron subsystem thermalizes, the material's intraband optical properties can be well described by the classical Drude model [1].

4.3.1 The Drude Permittivity and Plasma Frequency

In this regime, the transient complex dielectric permittivity ϵ of the metal at the probe laser frequency ω is mathematically expressed as:

$$\epsilon(T_e, T_l) = \epsilon_\infty - \frac{\omega_p^2(T_l)}{\omega(\omega + i\gamma(T_e, T_l))} \tag{4.2}$$

where ϵ_∞ represents the high-frequency background permittivity (accounting for interband transitions), $\omega_p(T_l)$ is the temperature-dependent plasma frequency, and $\gamma(T_e, T_l)$ is the total electron relaxation collision rate [26].

While the scattering rate γ is highly dynamic, the plasma frequency ω_p is solely influenced by the lattice temperature T_l. This dependence arises purely from the thermal volume expansion of the crystal lattice, which physically dilutes the free conduction band electron density n_e [26]. The expanded plasma frequency is given by:

$$\omega_p^2(T_l) = \frac{e^2 n_e(T_0)}{\epsilon_0 m_{\text{eff}}(1 + \beta\Delta T_l)} \tag{4.3}$$

where e is the elementary charge, ϵ_0 is the vacuum permittivity, m_{eff} is the effective electron mass, $n_e(T_0)$ is the unperturbed free electron density at ambient temperature, β is the volumetric thermal expansion coefficient, and ΔT_l is the transient increase in lattice temperature [26].

Crucially, because the volumetric thermal expansion coefficient β for noble and transition metals is extremely small (typically on the order of 10^{-5} K^{-1}), and ΔT_l is usually limited to a few tens of degrees during these experiments, the expansion term $\beta \Delta T_l \ll 1$. As a result, the plasma frequency $\omega_p(T_l)$ hardly varies. Therefore, the transient optical response observed in the Drude regime is almost entirely driven by drastic changes in the scattering rate, γ [26].

4.3.2 Temperature-Dependent Scattering and Reflectivity

The total electron collision rate γ acts as severe friction for the conduction electrons and is a dynamic function of both the electron and lattice temperatures:

$$\gamma(T_e, T_l) = \gamma_{e-e}(T_e) + \gamma_{e-ph}(T_l) \tag{4.4}$$

The first component, the electron-electron scattering rate (γ_{e-e}), scales quadratically with the electron temperature ($\propto T_e^2$) as predicted by Fermi Liquid theory [3, 26]. Consequently, immediately after thermalization when T_e is at its maximum, this T_e^2 dependence drives a massive spike in the scattering rate. The second component, the electron-phonon scattering rate (γ_{e-ph}), represents collisions between the electrons and the vibrating atomic lattice, scaling linearly with the lattice temperature ($\propto T_l$). As the electrons cool down and transfer their excess heat to the lattice, T_e drops but T_l rises. The increasing lattice temperature amplifies atomic vibrations, providing more obstacles for the electrons and sustaining a high scattering rate even as the electron bath cools [26].

By altering both the real and imaginary parts of the dielectric permittivity in Equation 4.2, this pump-induced spike in scattering friction ultimately manifests macroscopically through the Fresnel equations as the sharp decrease (the characteristic 'dip') observed in the transient optical reflectivity signal.

4.3.3 Phenomenological Modeling of the $\Delta R/R$ Signal

To quantitatively extract the characteristic time constants associated with the ultrafast heating and subsequent cooling mechanisms, the measured differential reflectivity dynamics can be reproduced using a widely adopted phenomenological model. Rather than relying on highly convoluted, nested exponential terms that can obscure the individual physical processes, a more direct and physically intuitive approach isolates the initial signal rise from the subsequent multi-exponential decay [27].

To accurately account for the finite temporal duration of the probing laser pulses, the intrinsic material response is convolved with the Gaussian cross-correlation $G(t)$ of the pump and probe pulses. The transient reflectivity is thus modeled as a biexponential decay modulated by an initial exponential rise function [27]:

$$\frac{\Delta R}{R}(t) = \left[\left(A_0 + A_1 e^{-t/\tau_1} + A_2 e^{-t/\tau_2}\right) \times \left(1 - e^{-t/\tau_{rise}}\right)\right] \otimes G(t) \tag{4.5}$$

This straightforward equation distinctly maps the sequential thermodynamic stages of the material following femtosecond excitation [1, 27]:

- τ_{rise} **(Ultrafast Rise Time):** The multiplicative factor $(1 - e^{-t/\tau_{rise}})$ dictates the ultrafast initial rise of the signal. It represents the characteristic timescale required for the highly energetic, non-equilibrium photoexcited electrons to scatter internally and establish a well-defined, thermalized Fermi-Dirac distribution with an elevated electron temperature (T_e) [1].
- τ_1 **(Fast Relaxation Time):** The primary exponential decay constant (τ_1, corresponding to amplitude A_1) characterizes the sub-picosecond to few-picosecond window. During

this phase, the hot thermalized electron bath transfers its excess energy to the colder atomic lattice via electron-phonon coupling, leading to a rapid macroscopic cooling of the electronic subsystem [27].

- τ_2 **(Slow Thermal Relaxation Time):** The secondary exponential decay constant (τ_2, corresponding to amplitude A_2) represents the long recovery tail. At this stage, the electrons and lattice have reached a localized thermal equilibrium ($T_e = T_l$), and the signal slowly decays over tens to hundreds of picoseconds as macroscopic heat diffuses out of the probed volume and into the underlying bulk substrate [26].

- A_0 **(Constant Background):** An amplitude offset accounting for any residual, long-lived thermal accumulation that does not dissipate within the measured pump-probe delay window [27].

4.3.4 Deviations from the Biexponential Model

It is important to emphasize that while Equation 4.5 provides a baseline for simple metals, the transient optical response is not universally biexponential. Depending on the specific material properties, structural geometry, and excitation fluence, the required fitting functions can become significantly more complex:

Oscillatory Terms (Coherent Phonons): In many pump-probe reflectivity experiments, the exponential decay is accompanied by pronounced damping oscillations superimposed on the background signal [2]. These oscillations arise from the generation and propagation of coherent acoustic phonon wavepackets (strain waves) that travel back and forth within the film or into the substrate, leading to Brillouin scattering of the probe pulse [2, 25]. Consequently, an additional damped sinusoidal term (e.g., $\propto \sin(\omega_c t)e^{-t/\tau_{damp}}$) must often be added to the phenomenological fit to capture this opto-acoustic interference.

Tri-Exponential Fits and Type I / Type II Dynamics: For ferromagnetic metals, the optical and magneto-optical signals reflect a complex energy flow governed by the Three-Temperature Model (3TM), where energy is shared among electrons, the lattice, and the spin bath. Depending on the material's magnetic specific heat and the ambient temperature relative to the Curie temperature (T_C), the dynamics are formally classified into two regimes [7]. *Type I* materials exhibit a rapid demagnetization followed by a distinct recovery, while *Type II* materials (or materials excited at highly elevated fluences) exhibit a slower, two-step demagnetization where the recovery time becomes indefinitely long [7, 9]. Because of this complex interplay, analytical solutions to the 3TM often manifest as either two-exponential or three-exponential decay functions [3]. Therefore, in highly coupled magnetic systems, a simple biexponential Drude relaxation is insufficient, and tri-exponential functions are frequently employed to accurately separate the distinct electron, lattice, and spin thermalization channels [3].

4.4 Advanced Modeling: The Role of Non-Thermal Electrons

4.4.1 Limitations of Standard Temperature Models

While the Two-Temperature Model (TTM) and Three-Temperature Model (3TM) provide an excellent phenomenological framework for describing the delayed relaxation dynamics of metals, they systematically fail at the earliest pump-probe delays (typically $t < 1$ ps) [9, 28]. The fundamental flaw in the standard TTM and 3TM lies in the assumption that the absorbed laser energy instantaneously creates a thermalized electron gas governed by Fermi-Dirac statistics [3, 28].

In reality, the initial optical excitation promotes electrons from below the Fermi level (E_F) to unoccupied states above it, creating a highly energetic, non-equilibrium population known

as non-thermal (NTH) electrons [3, 9]. Because the standard models ignore the finite time required for these NTH electrons to thermalize via electron-electron scattering, they predict an immediate peak in the electron temperature (T_e) at exactly zero delay. This leads to a severe overestimation of the early electronic temperature and fails to accurately reproduce the complex, often non-trivial rise dynamics observed in transient reflectivity ($\Delta R/R$) signals [28].

4.4.2 The Extended Three-Temperature Model (E3TM)

To resolve this discrepancy, the Extended Three-Temperature Model (E3TM) explicitly treats the non-thermal electrons as an independent, fourth energy reservoir [3, 9]. When the femtosecond laser pulse irradiates the metal, its energy strictly populates the NTH electron bath first. This non-thermal bath then acts as an active source, continuously transferring its energy to the thermal electrons (T_e), the spin subsystem (T_s), and the atomic lattice (T_l) [9].

The temporal evolution of the energy flow in the E3TM is governed by a system of four coupled differential equations [9]:

$$\frac{dN}{dt} = p(t) - p_e(t) - p_l(t) - p_s(t) \tag{4.6}$$

$$C_e(T_e)\frac{dT_e}{dt} = p_e(t) - G_{el}(T_e - T_l) - G_{es}(T_e - T_s) \tag{4.7}$$

$$C_l(T_l)\frac{dT_l}{dt} = p_l(t) - G_{el}(T_l - T_e) - G_{ls}(T_l - T_s) - K_l(T_l - 300)^3 \tag{4.8}$$

$$C_s(T_s)\frac{dT_s}{dt} = p_s(t) - G_{es}(T_s - T_e) - G_{ls}(T_s - T_l) \tag{4.9}$$

Here, N is the energy density of the optically pumped non-thermal electrons, and $p(t)$ represents the Gaussian temporal profile of the pump laser source. The parameters C_i and T_i denote the specific heat capacities and temperatures of the thermal electrons (e), lattice (l), and spins (s). The parameters G_{el}, G_{es}, and G_{ls} are the standard thermal energy exchange coefficients between the respective subsystems.

The critical addition in the E3TM is the energy flow rates $p_i(t)$ from the NTH electron bath into the thermal subsystems, defined as:

$$p_i(t) = \frac{G_{ei}}{C_e}N \quad \text{for } i \in \{e, l, s\} \tag{4.10}$$

where G_{ee} represents the specific energy exchange coefficient between the non-thermal electrons and the thermalized electron bath [9]. Finally, the K_l term in Equation 4.8 accounts for macroscopic thermal diffusion out of the lattice into the surrounding environment (substrate) [9].

4.4.3 The Role of Non-Thermal Electrons (τ_N) in the Signal Rise

By explicitly tracking the NTH electron density N, the E3TM provides a highly accurate map of the ultrafast signal rise. The characteristic decay time of the non-thermal electron population, denoted as τ_N, is effectively inversely proportional to the energy exchange coefficient G_{ee} [9].

Experimental observations and E3TM fits reveal that τ_N is heavily dependent on the pump fluence. At low laser fluences, G_{ee} is exceptionally large, meaning NTH electrons rapidly thermalize, and their overall contribution to the optical signal is minimal. However, as the pump fluence increases, G_{ee} decreases significantly, stretching τ_N to longer timescales (up to ~ 1 ps) [9]. This delayed thermalization occurs because the highly energetic non-thermal distribution limits the efficiency of electron-electron Coulomb scattering via Pauli blocking and modifications to the scattering phase space.

This prolonged survival of NTH electrons fundamentally alters the measured optical signals:

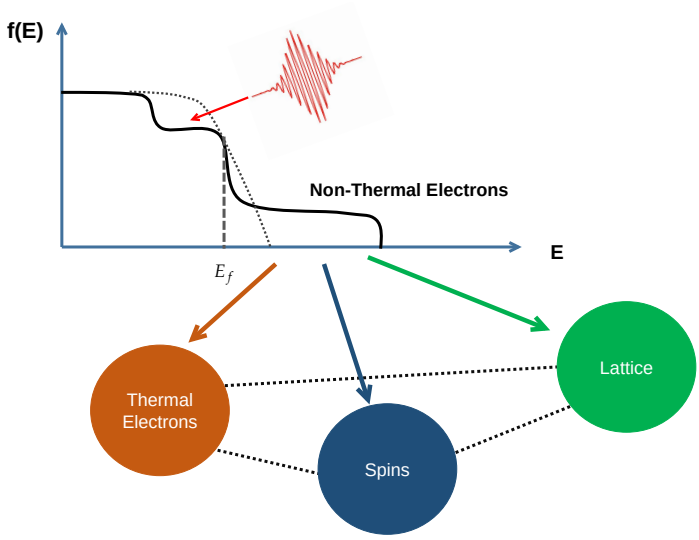

Figure 4.1: Schematic of energy transfer in the Extended Three-Temperature Model (E3TM). The laser pulse $p(t)$ directly populates the non-thermal electron bath (N). Energy subsequently flows from the NTH electrons into the thermal electrons (T_e), lattice (T_l), and spin (T_s) subsystems at rates governed by the coupling parameters G_{ei}. (Adapted from Shim et al. [9]).

- **Transient Reflectivity ($\Delta R/R$):** The $\Delta R/R$ signal is exceptionally sensitive to the parameter G_{ee} and the presence of non-thermal electrons. At high fluences, the surviving NTH population heavily modifies the optical state-filling (bleaching) effect, creating a non-trivial 'bump' or delayed secondary dip in the $\Delta R/R$ rise dynamics before classical thermal decay begins [9].
- **Magneto-Optical Kerr Effect (TR-MOKE):** Interestingly, E3TM analysis demonstrates that the TR-MOKE signal is relatively insensitive to the exact thermalization rate G_{ee} of the non-thermal electrons. However, the *amount* of energy transferred from the NTH bath to the spin subsystem ($p_s(t)$) dictates whether the magnetic system undergoes a rapid Type I demagnetization (where net energy quickly flows out of the spins) or a delayed Type II demagnetization (where the strong NTH energy tail sustains the demagnetized state) [9].

Because TR-MOKE alone is blind to the exact thermalization rate of the non-thermal bath, simultaneously measuring $\Delta R/R$ is absolutely crucial to lock in the E3TM parameters and accurately extract the true electron, spin, and lattice temperatures [9].

Chapter 5

Ultrafast Dynamics in Nickel Thin Films

5.1 Fundamental Properties of Ferromagnetic Nickel

As a prototypical itinerant $3d$ ferromagnet, Nickel (Ni) has served as the foundational cornerstone for understanding the ultrafast interactions between electron, spin, and lattice degrees of freedom [2, 3]. To accurately interpret the transient optical and magneto-optical responses of Ni thin films under femtosecond laser irradiation, it is first necessary to define its intrinsic electronic structure, optical excitation pathways, and magnetic anisotropy. Nickel follows **Type I** demagnetization dynamics [7].

Acknowledgement:
I express my sincere gratitude to Prof. Partha Mitra and Mr. Harekrishna Bhunia from the Spintronics Lab for their generosity in providing the necessary samples.

5.1.1 Electronic Configuration and Band Structure

The ground-state electronic configuration of Nickel is [Ar] $3d^8 4s^2$. Unlike localized magnetic systems (such as the $4f$ electrons in rare-earth metals), the magnetic moment in Ni arises entirely from its itinerant, delocalized $3d$ valence electrons [7]. Due to exchange interactions, the $3d$ energy band is split into majority (spin-up) and minority (spin-down) subbands. Because the Fermi level ($E_F \approx 5.1$ eV) intersects the top of the minority $3d$ band while the majority $3d$ band is fully occupied, an imbalance in the spin population occurs. This specific distribution of holes in the minority band yields a net atomic magnetic moment of $\sim 0.6\mu_B$ per atom [7, 28]. Consequently, the density of states (DOS) in Ni exhibits a massive asymmetry, with a sharp peak of available minority $3d$ states sitting immediately above the Fermi level [3, 28].

5.1.2 Optical Excitation and Thermomodulation

In our two-color pump-probe experiments, the Ni system is driven violently out of equilibrium by a 400 nm (3.1 eV) femtosecond pump pulse. Because the necessary excitation energy to bridge the $3d$ states to the Fermi level is only $\sim 0.1 - 0.8$ eV, the highly energetic 3.1 eV pump photons easily promote electrons from deeply occupied d-states well below E_F to unoccupied, highly mobile sp-states high above E_F [29]. This massive injection of energy creates a highly

non-thermal electron distribution that rapidly alters the exchange splitting (ΔE_{ex}) and triggers violent spin-flip scattering events, leading to a sudden reduction in the macroscopic spin population [3].

To monitor the subsequent thermodynamic relaxation, an 800 nm (1.55 eV) delayed probe pulse interrogates the sample. The measured transient differential reflectivity ($\Delta R/R$) specifically tracks the thermomodulation of the material's complex dielectric function [1]. At 1.55 eV, the optical response of Ni is governed by a combination of the free-carrier Drude response and interband Lorentz oscillator transitions [1, 28]. As established in the previous chapter, the pump-induced heating spikes the electron and lattice temperatures (T_e and T_l), which in turn drastically increases the electron collision rate (γ). By modifying both the real and imaginary parts of the permittivity tensor (as detailed previously in Equation 4.2 and Equation 4.4), this thermal friction manifests as the characteristic $\Delta R/R$ signal, allowing us to optically map the electron-phonon thermalization [1, 26].

5.1.3 Magnetic Anisotropy and Domains in Thin Films

While bulk Ni exhibits intrinsic magnetocrystalline anisotropy, the magnetic orientation in ultrathin Ni films ($\sim 10-20$ nm) is dictated by a strict competition between various anisotropy energy terms [3, 5]. In such nanometer-scale geometries, the dominant factor is typically the shape anisotropy energy ($2\pi M_s^2$), arising from dipole-dipole interactions, which strongly forces the macroscopic magnetization to lie entirely within the film plane.

However, this in-plane preference is not absolute. The introduction of symmetry-breaking at the interfaces (surface anisotropy) or the presence of significant epitaxial strain can counteract the shape anisotropy. For instance, Ni films grown on a Sapphire substrate undergo lattice mismatch, inducing magneto-elastic strain [2]. Depending on the exact film thickness and the quality of the crystalline interfaces, this strain can generate a strong perpendicular magnetic anisotropy (PMA) component, potentially pulling the magnetization out of the film plane or creating complex, multi-domain magnetic textures that dictate the efficiency of spin-current generation [3, 5].

5.2 Sample Fabrication and Optical Characterization

To experimentally investigate the ultrafast demagnetization and structural dynamics discussed in the previous sections, a highly specific multilayer thin film architecture was required. The physical dimensions and interface qualities of the sample play a critical role in dictating the optical absorption, strain propagation, and magnetic anisotropy of the Nickel layer.

5.2.1 Thin Film Structure and Deposition

The sample investigated in this study is a symmetric metallic trilayer deposited onto a transparent dielectric substrate. The specific heterostructure consists of **Cr (∼2 nm) / Ni (∼10 nm) / Cr (2 nm)** grown on a Sapphire substrate. The metallic layers were deposited utilizing Electron Beam Evaporation, a technique that allows for precise control over the deposition rate and thickness of ultrathin films.

Each layer in this architecture serves a distinct physical purpose:

- **Bottom Cr Seeding Layer (2 nm):** Transition metals often suffer from poor adhesion and severe lattice mismatch when grown directly on bare oxide substrates like Sapphire. The bottom Chromium layer acts as a vital seeding and adhesion layer, bridging the structural gap between the Sapphire substrate and the ferromagnetic Nickel film to promote uniform planar growth.

- **Active Ni Layer (∼10 nm):** This is the primary ferromagnetic layer under investigation. At ∼10 nm, the shape anisotropy dominates, forcing the macroscopic magnetization to lie preferentially in the film plane, while remaining thin enough to be uniformly excited by the skin-depth of the femtosecond pump pulse.
- **Top Cr Passivating Layer (∼2 nm):** Ultrathin Nickel films are highly reactive and will rapidly degrade and oxidize when exposed to ambient atmospheric conditions, which can severely alter their magnetic and optical properties [29]. The top Chromium layer acts as a sacrificial capping layer. Upon exposure to air, it naturally oxidizes to form a stable, protective layer of Chromium(III) oxide (Cr_2O_3), acting as an effective passivation barrier that seals the pristine Ni layer beneath it.

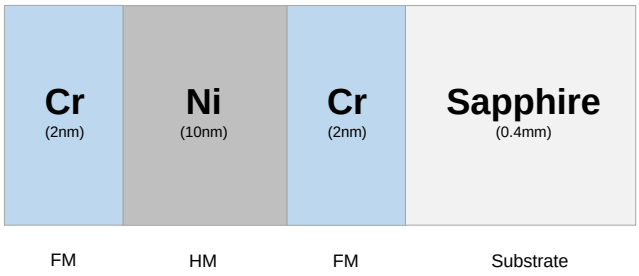

Figure 5.1: Schematic representation of the fabricated Cr($\sim 2nm$) / Ni($\sim 10nm$) / Cr($2nm$) sample on a Sapphire substrate. The active ferromagnetic Ni layer is sandwiched between a bottom Cr seeding layer and a top Cr layer that oxidizes (Cr_2O_3) to serve as a protective passivation barrier.

5.2.2 Linear Optical Properties at 800 nm

Before conducting the time-resolved pump-probe measurements, the baseline linear optical properties of the unperturbed sample were characterized. A low-power continuous wave (CW) laser operating at a wavelength of 800 nm (photon energy of $\sim$ 1.55 eV) with an average power of 50 μW was utilized to measure the macroscopic optical response.

The sample exhibited a transmittance (T) of approximately 32% and a reflectance (R) of approximately 36%. By applying the fundamental energy conservation relation for thin-film optical systems ($A = 1 - R - T$) [5], we can accurately determine the optical absorptance (A) of the metallic heterostructure. For the 800 nm wavelength, the absorptance is calculated to be $\sim$ 32%.

This substantial absorptance confirms that a significant fraction of the incident laser energy is efficiently deposited into the electron bath of the metallic layers. When subjected to the intense femtosecond pump pulses in our transient experiments, this 32% absorption fraction dictates the initial non-equilibrium energy density (N) injected into the system, driving the severe electron temperature (T_e) spike and triggering the subsequent thermomodulation of the dielectric function (as defined in Equation 4.2) and the ultrafast demagnetization processes.

5.3 Experimental Methodology and Data Extraction

Before analyzing the fluence-dependent ultrafast dynamics of the Nickel thin films, it is necessary to detail the specific experimental beam parameters and the rigorous methodology used to

extract the true static reflectivity (R), which is required to accurately calculate the differential signal ($\Delta R/R$).

5.3.1 Pump-Probe Parameters and Beam Spot Sizes

The transient reflectivity measurements were conducted using the degenerate 400 nm pump / 800 nm probe configuration detailed in the previous chapter. To ensure uniform excitation across the probed region and avoid edge effects, the spatial profile of the pump beam was configured to be strictly larger than the probe beam [25]. Based on spatial beam profiling, the pump beam diameter was set to ~ 50 μm, while the delayed probe beam was focused to a smaller diameter of ~ 38 μm. These spot sizes were utilized to precisely calculate the incident laser fluences, which were systematically varied from 0.216 mJ/cm^2 up to 1.728 mJ/cm^2 for the following fluence-dependent studies.

5.3.2 Static Reflectivity (R) Measurement and Extrapolation

In standard pump-probe spectroscopy, the lock-in amplifier extracts the minute change in reflected probe intensity (ΔR). To normalize this and obtain the physically meaningful fractional change ($\Delta R/R$), the absolute static reflectivity (R) of the sample under the exact experimental conditions must be known.

Directly measuring R during the transient experiment poses a technical challenge due to the specific sensitivity settings of the transimpedance (current) amplifier. For our time-resolved measurements, the amplifier was set to a highly sensitive gain (e.g., 50 mV/nA) to resolve the tiny ΔR signal. However, if we simply block the pump and attempt to measure the static probe reflection at this exact sensitivity by placing an optical chopper in the probe path, the massive static signal completely saturates the amplifier.

To bypass this saturation and extract the true R, we utilized a logarithmic extrapolation technique. The probe chopper was activated, and the static reflection signal (in mV) was recorded across a range of lower, non-saturating amplifier sensitivities. Because the signal scales linearly with the amplifier gain, we plotted the logarithm of the amplifier sensitivity against the measured signal voltage. By performing a linear fit on this log-scaled data, we could accurately extrapolate the precise baseline voltage corresponding to the static reflectivity R at the experimental 50 mV/nA sensitivity setting.

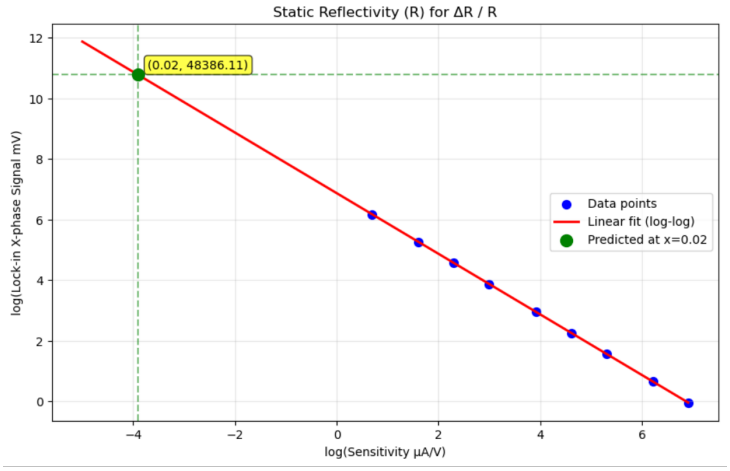

Figure 5.2: Log-linear extrapolation of the static reflectivity signal. By measuring the chopped probe signal at various lower current amplifier sensitivities and plotting the log of the sensitivity versus the measured voltage, the true static reflectivity (R) at the highly sensitive experimental setting (50 mV/nA) is accurately extracted.

5.4 Fluence-Dependent Transient Reflectivity of Nickel

5.4.1 Raw $\Delta R/R$ Dynamics and Coherent Phonons

Figure 5.3 illustrates the raw, zero-corrected transient differential reflectivity ($\Delta R/R$) of the Nickel sample as a function of pump fluence. As expected from the thermomodulation of the dielectric function, an increase in the incident pump fluence deposits more energy into the electron bath, leading to a proportionally larger drop (negative dip) in the $\Delta R/R$ signal [1].

Beyond the primary electronic decay, a highly prominent secondary feature emerges at higher fluences: distinct oscillations superimposed on the recovery tail. As highlighted in the zoomed-in inset of Figure 5.3, these oscillations are largely absent at the lowest fluence of 0.216 mJ/cm^2. However, as the fluence increases, the amplitude of these oscillations grows significantly, reaching a maximum at 1.728 mJ/cm^2.

These oscillatory features are generally attributed to the generation of coherent acoustic phonons within the material [2, 28]. When the intense laser pulse rapidly heats the Ni lattice, it triggers impulsive thermoelastic stress that launches acoustic phonon wavepackets. These phonons dynamically modulate the optical properties of the film, leading to the observed periodic ringing in the transient reflectivity signal. In metallic thin films, such coherent phonons can often manifest as standing waves confined within the film boundaries [2]. However, because the precise origin of these vibrations, whether they are standing waves isolated within the Ni layer or propagating modes interacting with the underlying Sapphire substrate, cannot be definitively assigned from the raw visual data alone, a rigorous theoretical fitting and strain propagation analysis will be presented in subsequent sections to support these arguments and exactly determine the nature of the oscillations.

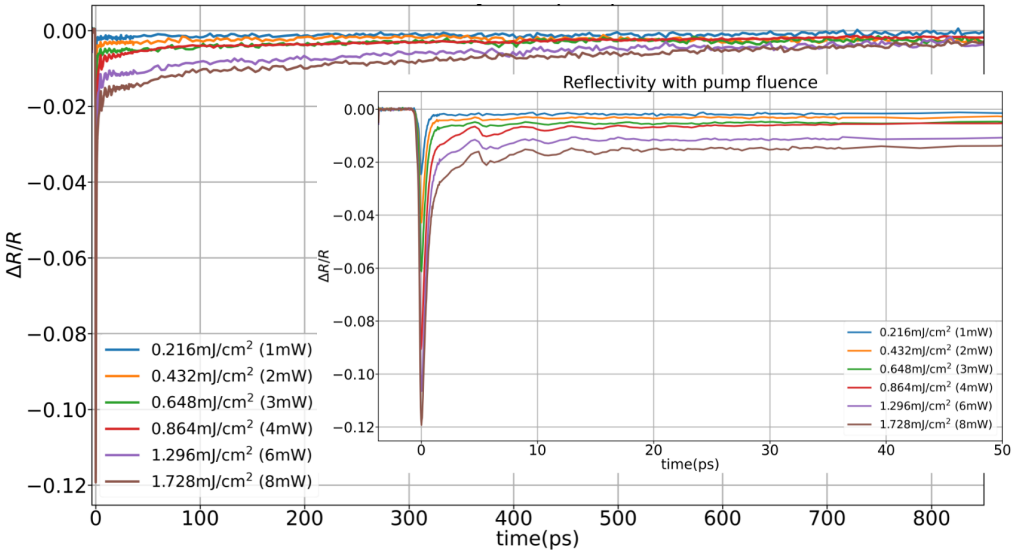

Figure 5.3: Raw zero-corrected transient reflectivity ($\Delta R/R$) of the Ni thin film at varying pump fluences (0.216 to 1.728 mJ/cm^2). The depth of the electronic dip increases with fluence. The inset provides a zoomed-in view of the recovery tail, clearly showing the emergence of chirped coherent acoustic phonon oscillations at higher fluences, which are absent at the lowest fluence.

5.4.2 Cross-Phase Modulation (XPM) and the Coherent Artifact

Before analyzing the thermal relaxation timescales, it is critical to address the earliest feature of the pump-probe signal. As seen immediately behind (or preceding) the primary electronic

rise peak, there is a sudden, sharp, and highly transient spike or 'jump' in the signal precisely at zero delay ($t \approx 0$).

This instantaneous spike is not of thermal or magnetic origin; rather, it is a non-linear optical phenomenon known as the coherent artifact [1]. Because the intense 400 nm pump and 800 nm probe pulses are spatially and temporally overlapped inside the sample, their combined electric fields interact through the third-order non-linear susceptibility ($\chi^{(3)}$) of the material and the surrounding interfaces [1]. This instantaneous interaction leads to Cross-Phase Modulation (XPM) and two-photon absorption processes, causing a transient modulation of the probe's phase and amplitude that exists only for the exact duration of the pump-probe cross-correlation [1]. This XPM spike must be carefully decoupled from the true electronic rise time (τ_{ee}) during data fitting.

5.4.3 Normalized Dynamics and Relaxation Timescales

To directly compare the thermal relaxation timescales (τ) independent of the varying signal magnitudes, the $\Delta R/R$ traces were normalized such that all minimum peak heights are fixed to -1 (Figure 5.4).

This normalization reveals two critical temporal trends:

1. **Constant Rise Time:** The ultrafast rise time of the signal remains remarkably independent of the pump fluence. This implies that the initial electron-electron thermalization timescale (τ_{ee}) is dominated by the prompt pulse width and the intrinsic massive density of states at the Fermi level in Nickel, rather than the absolute number of excited carriers, with $\tau_{rise} < 100fs$ which is close to the pulse width.

2. **Slower Decay at High Fluence:** In stark contrast, the recovery tail (governed by τ_{ep} and τ_{th}) exhibits a clear fluence dependence. As the fluence increases, the normalized decay becomes progressively slower. This deceleration is a direct consequence of the elevated initial electron temperature (T_e). Because the electronic heat capacity (C_e) in metals is linearly proportional to T_e, higher fluences massively increase C_e [9, 28]. Consequently, the hotter electron bath holds more thermal energy and requires significantly more time to transfer this heat to the lattice, thereby stretching the observed electron-phonon relaxation time (τ_{ep}).

5.4.4 Spatio-Temporal 2D Mesh Representations

To provide a comprehensive overview of the entire dataset, the fluence-dependent dynamics are compactly visualized using 2D spatio-temporal Mesh plots. Figure 5.5 presents these mesh plots side-by-side: the left panel displays the raw $\Delta R/R$ amplitude, explicitly highlighting the massive increase in absorbed energy at higher fluences, while the right panel displays the normalized $\Delta R/R$, perfectly isolating the temporal broadening (slower τ decay) and the onset of the coherent phonon oscillations as fluence increases.

5.5 Phenomenological Modeling and Relaxation Timescales

To quantitatively extract the underlying electron, lattice, and strain dynamics from the raw transient reflectivity ($\Delta R/R$) data, a comprehensive phenomenological model is required. As observed in the normalized data (Figure 5.4), the complex recovery tail cannot be described by a simple exponential decay due to the prominent superposition of opto-acoustic interference.

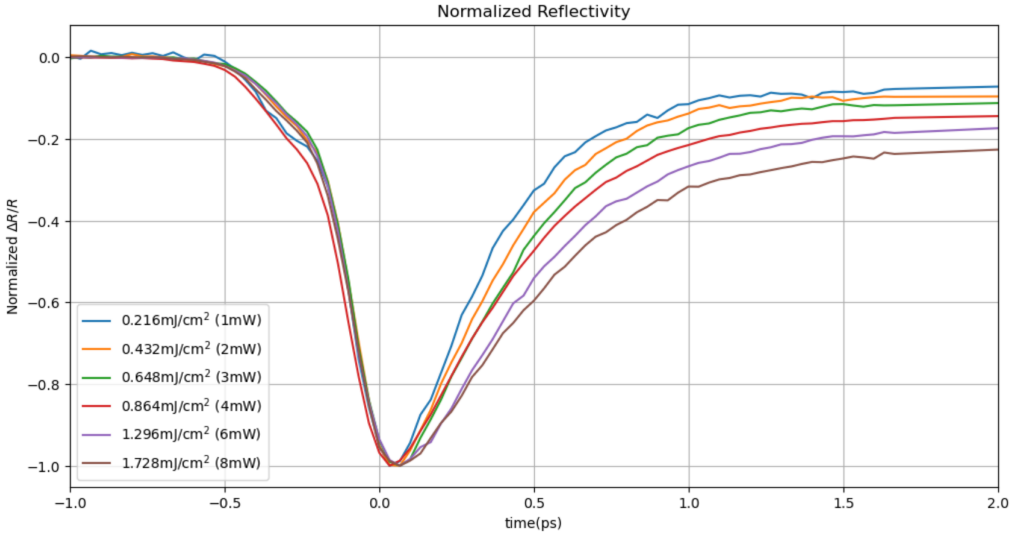

Figure 5.4: Normalized transient reflectivity ($\Delta R/R$) dynamics, with all peak minima scaled to -1. The data clearly demonstrates a fluence-independent rise time, a distinct Cross-Phase Modulation (XPM) coherent artifact near zero delay, and a progressively slower recovery decay at higher fluences.

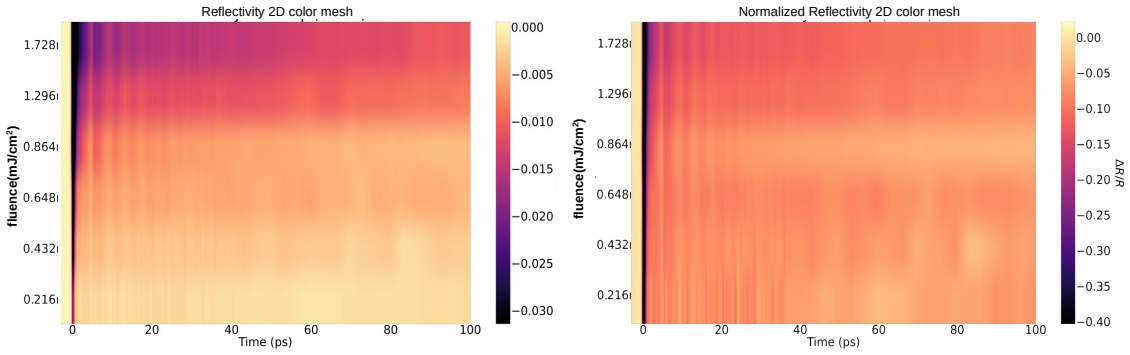

Figure 5.5: 2D color mesh of the transient reflectivity as a function of pump-probe delay and incident fluence. **Left:** Raw $\Delta R/R$ demonstrating the increasing depth of the thermomodulation signal. **Right:** Normalized $\Delta R/R$ highlighting the invariant rise time and the delayed cooling (slower decay) at elevated fluences.

5.5.1 The Multi-Component Fitting Function

The fluence-dependent $\Delta R/R$ traces were rigorously fitted using a multi-component mathematical function that isolates the electronic/thermal relaxation from the coherent acoustic phonon responses [2, 25]. The complete fitting equation is defined as:

$$\begin{aligned}\frac{\Delta R}{R}(t) = &\left[A_1 e^{-t/\tau_1} + A_2 e^{-t/\tau_2}\right] + C_0 \\ &+ A_{\text{long}} e^{-t/\tau_{\text{long}}} \sin(2\pi f_{\text{long}} t + \phi_{\text{long}}) \\ &+ A_{\text{osc}} e^{-t/\tau_{\text{osc}}} \sin\left(2\pi(f_{\text{osc}} + \beta t)t + \phi_{\text{osc}}\right)\end{aligned} \tag{5.1}$$

This model comprises four distinct physical contributions:

1. **Biexponential Thermal Decay (A_1, τ_1, A_2, τ_2):** Represents the two-step thermodynamic cooling of the system. The fast component (τ_1) corresponds to the electron-phonon thermalization, while the slower component (τ_2) corresponds to macroscopic heat diffusion [1].

2. **Constant Offset (C_0):** Accounts for any residual, long-lived thermal accumulation that does not dissipate within the measured pump-probe delay window [25].

3. **Slow Acoustic Oscillation ($A_{\text{long}}, f_{\text{long}}$):** A low-frequency sinusoidal component ($\sim$ 1.5 GHz) that remains relatively fixed across fluences, typically associated with deep-penetrating strain waves[2].

4. **Fast Chirped Acoustic Oscillation ($A_{\text{osc}}, f_{\text{osc}}$):** A highly damped, high-frequency ($\sim$ 24 GHz) sinusoidal component representing the primary coherent acoustic phonons within the thin film. To account for the frequency-varying nature of the early thermoelastic stress profile, a chirp rate parameter (β) is included [28].

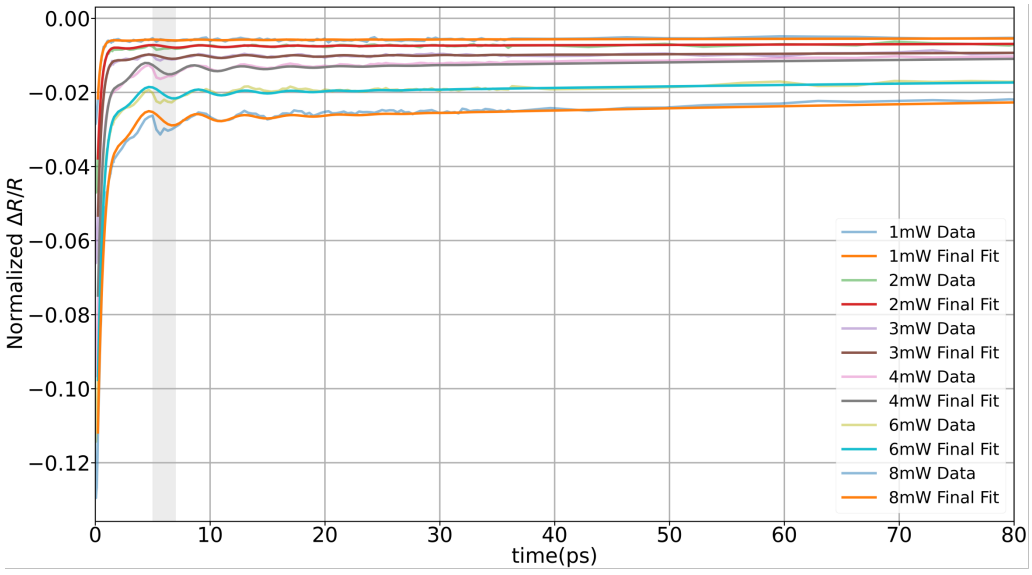

Figure 5.6: Representative quality of fit for the transient differential reflectivity data using the multi-component model described in Equation 5.1. The fit perfectly captures the initial biexponential decay, the chirped high-frequency oscillations, and the long thermal recovery tail.

5.5.2 Fluence Dependence of Electronic and Thermal Parameters

Applying this model across all measured fluences yields the parameter trends illustrated in Figure 5.7. Note that not all parameters exhibit distinct trends; for instance, the slow decay time τ_2 fluctuates randomly around 210 ± 50 ps, indicating that the long-term macroscopic heat diffusion to the substrate is relatively insensitive to the initial excitation density in this regime. Similarly, the slow oscillatory parameters remain largely constant ($f_{\text{long}} \approx 1.5$ GHz, $A_{\text{long}} \approx 5 \times 10^{-4} \pm 0.3$).

However, the primary electronic relaxation parameters (τ_1, A_1, A_2) exhibit strict, physically meaningful fluence dependencies:

- **Amplitude of Fast Decay (A_1):** The amplitude A_1 exhibits a distinct power-law increase with rising pump fluence. This non-linear scaling originates from the temperature dependence of the Drude collision rate. As demonstrated by Block et al., the electron-electron scattering rate scales quadratically with electron temperature ($\gamma_{ee} \propto T_e^2$) [26]. Because higher fluences generate a much hotter initial electron bath, this T_e^2 dependence drives a massive, non-linear spike in the scattering rate, proportionally amplifying the $\Delta R/R$ thermomodulation dip.

- **Slowing of Electron-Phonon Coupling (τ_1):** The fast relaxation time, τ_1, increases strictly linearly from ~ 0.3 ps at the lowest fluence to ~ 0.6 ps at the highest fluence. This linear slowing of the electron-phonon thermalization is a hallmark of the Two-Temperature Model (TTM) [9]. The electronic heat capacity (C_e) of a metal is not constant, but scales linearly with the electron temperature ($C_e = \gamma_e T_e$). Because higher fluences generate a much hotter initial electron bath, the heat capacity of the electron subsystem increases dramatically. Consequently, the "hotter" electrons hold more thermal energy and require a longer time to transfer it to the lattice via the electron-phonon coupling constant (G_{ep}), stretching τ_1 [28].

- **Slow Acoustic Oscillation (A_{long}, f_{long}):** It is likely related to deep-penetrating sonic waves propagating into the bulk substrate, consistent with observations in thick Ni crystals [2].

5.5.3 Fluence Dependence of Coherent Acoustic Phonons

The parameters extracted from the high-frequency chirped oscillation (A_{osc}, τ_{osc}, f_{osc}) provide deep insights into the thermoelastic strain generated within the Ni film.

As established visually in the previous section, the generation of coherent acoustic phonons requires a threshold of thermoelastic stress. This is quantitatively confirmed by the fitting results: for the first three (lowest) fluences, the amplitude of the oscillation (A_{osc}) is exceedingly small, rendering the extracted values for both A_{osc} and the damping time (τ_{osc}) untrustworthy and heavily influenced by background noise.

However, once the fluence exceeds this threshold, the acoustic parameters stabilize:

- **Constant Frequency (f_{osc}):** The primary oscillation frequency remains remarkably constant at approximately 24 GHz across all higher fluences. Because this frequency is fundamentally dictated by the longitudinal speed of sound in the material and the physical boundaries of the propagating medium (acting as an acoustic cavity), its invariance confirms that the elastic constants of the Ni film are not permanently altered or melted by the pump pulses [2].

- **Acoustic Damping (τ_{osc}):** For higher fluences, the acoustic damping time becomes fixed at approximately 6 ps. This rapid damping, combined with the consistent chirp rate ($\beta \approx 0.001$), suggests that the strain wavepacket is quickly exiting the primary detection

volume of the ultrathin Ni layer and propagating into the adjacent Chromium layers or the Sapphire substrate [28].

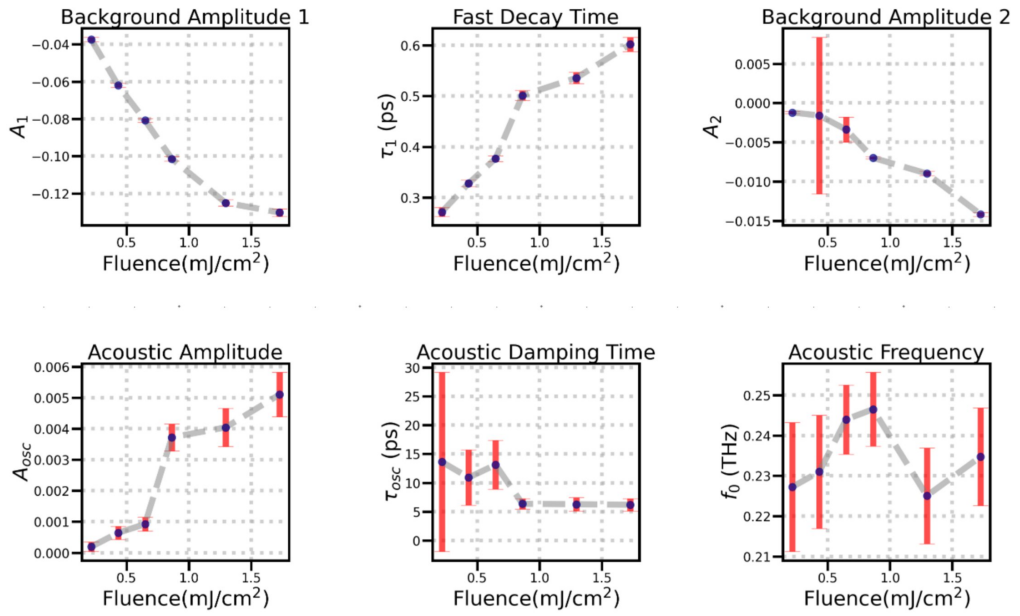

Figure 5.7: Extracted fitting parameters as a function of incident pump fluence. **Top Row:** The fast electronic amplitude (A_1) shows a power-law increase, while the electron-phonon relaxation time (τ_1) exhibits a linear increase from 0.3 to 0.6 ps. **Bottom Row:** The fast acoustic oscillation frequency (f_{osc}) remains constant at ~ 24 GHz. The acoustic amplitude (A_{osc}) and damping time (τ_{osc}) only stabilize at higher fluences once the thermoelastic stress threshold is overcome, fixing τ_{osc} at ~ 6 ps.

5.6 Origin and Damping of the Coherent Acoustic Phonons

As established in the fitting parameters (Figure 5.7), the primary oscillatory feature in the transient reflectivity data manifests with a frequency of $f_{\text{osc}} \approx 24$ GHz (corresponding to a time period of ~ 4.1 ps) and a remarkably fast damping time of $\tau_{\text{osc}} \approx 6$ ps. To physically justify these values and prove that these oscillations are coherent standing waves confined within the Nickel film, we must evaluate the thermoelastic mechanics and the acoustic impedance of the interfaces.

5.6.1 Pulse Period and the Breathing Mode

Following the absorption of the femtosecond pump pulse, the rapid thermalization of the electron and lattice subsystems establishes a highly localized temperature profile. As foundationaly described by Thomsen *et al.*, this impulsive heating generates an immense, instantaneous thermoelastic stress (σ_{th}) within the metal [30]. Because the laser spot size (~ 50 μm) is orders of magnitude larger than both the film thickness and the optical penetration depth, the resulting stress gradient is strictly one-dimensional along the surface normal (z-axis) [28, 30]. This one-dimensional stress acts as the driving force that launches coherent longitudinal acoustic phonons, which subsequently modulate the local optical constants and reflectivity of the film [30].

The specific temporal manifestation of these acoustic waves depends strongly on the ratio of the film thickness (d) to the optical penetration depth (ξ) of the pump pulse. As recently

demonstrated by Chauhan *et al.*, when a film is significantly thicker than the penetration depth ($d \gg \xi$), the localized stress launches Traveling Acoustic Strain Pulses (TASP) that bounce between the film interfaces, appearing in the time-domain as discrete, separated echo pulses [27].

However, in the case of our ultrathin 10 nm Ni film, the thickness is less than or comparable to the optical penetration depth of the 400 nm pump light ($d \lesssim \xi$). Consequently, the pump pulse homogeneously excites the entire film volume almost simultaneously [27]. In this regime, the discrete traveling pulses are replaced by continuous "oscillation-like" ringing because the entire metallic film acts as an Acoustic Phonon Resonator (APR) [27]. The ultrathin film cavity traps these longitudinal acoustic modes, creating a fundamental standing wave, often termed a "breathing mode" [2].

The acoustic period (T_{ac}) of this resonant breathing mode—or inversely, its fundamental resonant frequency (ν_{LA})—is determined by the round-trip travel time of the sound wave across the film cavity [2, 27]:

$$T_{ac} = \frac{1}{\nu_{LA}} = \frac{2d}{v_s} \tag{5.2}$$

where d is the thickness of the Ni film and v_s is the longitudinal speed of sound in Nickel. Given our nominal Ni film thickness of $d \approx 10$ nm and the accepted sound velocity for Ni ($v_s \approx 5.6$ nm/ps or 5600 m/s), the theoretical acoustic period is calculated as:

$$T_{ac} = \frac{2(10 \text{ nm})}{5.6 \text{ nm/ps}} \approx 3.6 \text{ ps}$$

This theoretical period of 3.6 ps (equivalent to a resonance frequency of ~ 27 GHz) is in excellent agreement with the experimentally observed continuous oscillation timescale of ~ 4.1 ps (24 GHz). The slight deviation in the experimental frequency is easily accounted for by the presence of the 2 nm Chromium seeding and passivating layers, which slightly increase the total acoustic cavity length and mass. This definitively confirms that the 24 GHz modulation is indeed the fundamental standing strain wave bouncing inside the metallic heterostructure acting as an acoustic phonon resonator.

5.7 Thermodynamic Modeling: The Two-Temperature and Rosei Models

While phenomenological multi-exponential fits successfully isolate the relaxation timescales and acoustic oscillations, explicitly determining the microscopic electron and lattice temperatures (T_e and T_l) requires coupling a thermodynamic heat transfer model to the optical response.

5.7.1 Energy Reservoirs and the Rosei Model

To map the measured fractional reflectivity ($\Delta R/R$) to the underlying subsystem temperatures, we must establish how the dielectric function responds to transient heating. As demonstrated by Groeneveld et al., based on the original theory by Rosei, when a metal is probed at photon energies below its main interband absorption threshold ($\hbar\omega < E_{ib}$), the pump-induced change in the dielectric function tracks the *Total Excess Energy* (ΔU) of the system rather than just the linear temperature change [31].

The total excess energy is partitioned into the electronic and lattice reservoirs, governed by their respective heat capacities. For transition metals like Nickel, the massive density of states at the Fermi level dictates that the electronic specific heat (C_e) is strictly linear with the electron temperature:

$$C_e(T_e) = \gamma_{Ni} T_e \tag{5.3}$$

where $\gamma_{Ni} \approx 1065\,\text{J} \cdot \text{m}^{-3} \cdot \text{K}^{-2}$ is the electronic specific heat constant for Nickel. In contrast, for ambient temperatures above the Debye temperature ($T > \Theta_D$), the lattice heat capacity

(C_l) approaches the classical Dulong-Petit limit and is assumed to be a large constant ($C_l \approx 3Nk_B$) [31].

Integrating these heat capacities from the ambient baseline temperature (T_0) yields the transient excess energies for the electron (ΔU_e) and lattice (ΔU_l) subsystems:

$$\Delta U_e(t) = \int_{T_0}^{T_e(t)} C_e(T)dT = \frac{1}{2}\gamma_{Ni}\left[T_e(t)^2 - T_0^2\right] \tag{5.4}$$

$$\Delta U_l(t) = \int_{T_0}^{T_l(t)} C_l dT = C_l\left[T_l(t) - T_0\right] \tag{5.5}$$

5.7.2 2TM Differential Equations and Opto-Thermal Scaling

The temporal evolution of T_e and T_l is governed by the standard Two-Temperature Model (2TM) coupled differential equations [31]:

$$C_e(T_e)\frac{dT_e}{dt} = -G_{el}(T_e - T_l) + P(t) \tag{5.6}$$

$$C_l\frac{dT_l}{dt} = +G_{el}(T_e - T_l) \tag{5.7}$$

where G_{el} is the electron-phonon coupling constant and $P(t)$ is the laser source term, approximated as a Gaussian pulse with a width of $\sigma \approx 60$ fs.

By uniting the 2TM thermodynamic simulation with the optical Rosei model, the experimental differential reflectivity data can be directly fitted using a linear combination of the excess energies. The final scaling equation linking the temperatures to the optical measurement is defined as:

$$\left(\frac{\Delta R}{R}\right)_{\text{fit}}(t) = \underbrace{A \cdot \left[T_e(t)^2 - T_0^2\right]}_{\text{Electronic (Drude/Rosei)}} + \underbrace{B \cdot \left[T_l(t) - T_0\right]}_{\text{Lattice (Strain/Expansion)}} \tag{5.8}$$

Here, the scaling constants A and B account for the specific probe sensitivity to the electron and lattice energy variations, respectively [31].

5.7.3 Extracted Temperature Dynamics and Parameters

Utilizing Equation 5.6, Equation 5.7, and Equation 5.8 (only background expoententials were fed as $\Delta R/R$), the fluence-dependent $\Delta R/R$ traces were numerically fitted to extract the underlying thermodynamic responses.

The results of these opto-thermal fits are laid out in the following figures. Figure 5.8 displays the temporal evolution of the calculated electron temperature (T_e) and lattice temperature (T_l) baths for all measured fluences, illustrating the massive initial spike in T_e and the subsequent thermal equilibration. Furthermore, Figure 5.9 presents the full suite of extracted fitting parameters across the fluence regime, including the electron-phonon coupling constant (G_{el}), the discrete relaxation time constants (τ_1, τ_2), the peak subsystem temperatures, the dynamic heat capacities (C_e, C_l), the lattice strain slope, and the explicit dependence of the coupling constant G_{el} on the peak initial electron temperature.

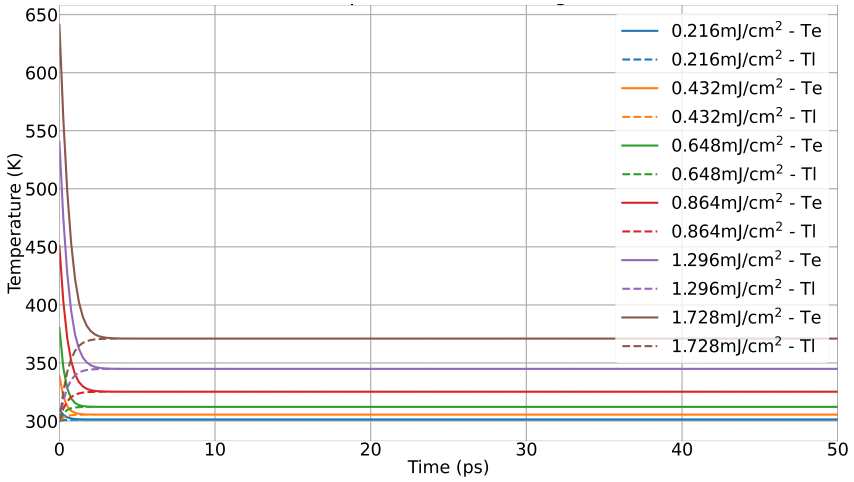

Figure 5.8: Fluence-dependent temporal evolution of the electron temperature (T_e, solid lines) and lattice temperature (T_l, dashed lines) extracted via the Two-Temperature Model.

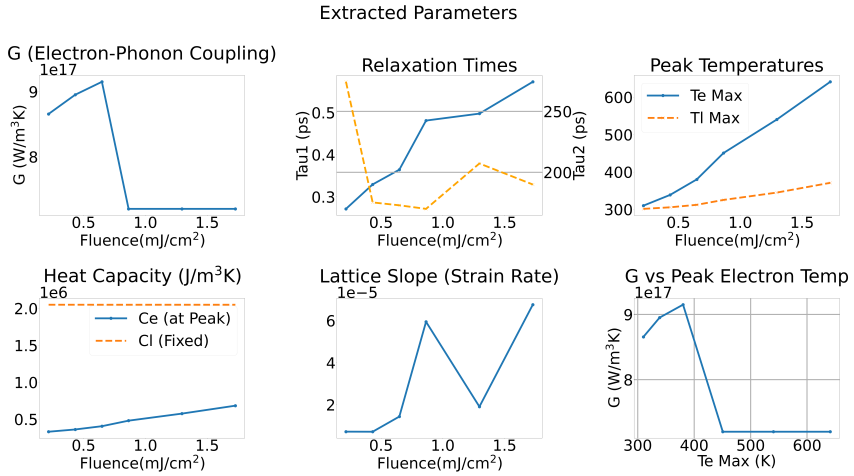

Figure 5.9: Extracted thermodynamic and optical scaling parameters from the 2TM-Rosei fits as a function of pump fluence. The panels detail the evolution of G_{el}, τ_1, τ_2, peak T_e and T_l, subsystem heat capacities (C_e, C_l), the lattice strain slope, and the specific relationship between G_{el} and the peak electron temperature.

Chapter 6

Ultrafast Dynamics in Pt/Fe Bilayer Spintronic Emitters

6.1 Introduction to Spintronic Terahertz Emitters

As detailed extensively in chapter 1 (Chapter 1), spintronic terahertz emitters (STEs) operate on the principles of ultrafast spin-current generation and subsequent spin-to-charge conversion. The intense optical excitation of the ferromagnetic layer creates a non-equilibrium distribution of carriers, launching a superdiffusive spin current. This spin current is injected into an adjacent heavy metal layer, where the strong spin-orbit coupling drives the Inverse Spin Hall Effect (ISHE), converting the longitudinal spin flow into a transverse transient charge current that radiates a broadband THz pulse.

Furthermore, we previously established that the Fe/Pt interface acts as an intrinsic spin filter, drastically enhancing the emission efficiency by allowing highly mobile majority spins to propagate while trapping minority spins. With these fundamental working mechanisms already covered, this chapter focuses directly on the specific structural characterization and the ultrafast transient reflectivity dynamics of the Pt/Fe bilayer system.

Acknowledgement:
I express my sincere gratitude to Prof. Sunil Kumar and the Femtosecond Spectroscopy and Nonlinear Photonics Laboratory at the Indian Institute of Technology (IIT) Delhi for their generosity in providing the necessary samples for this investigation.

6.2 Sample Characterization and Magnetic Anisotropy

6.2.1 Deposition and Crystallinity

The spintronic heterostructures utilized in this study were fabricated using ultra-high vacuum radio frequency (RF) magnetron sputtering onto fused quartz substrates [32]. According to reported X-ray Diffraction (XRD) measurements for films grown under these exact conditions, the deposited metallic layers exhibit a polycrystalline structure characterized by random crystal grain orientations [32].

6.2.2 Thickness-Dependent Magnetic Anisotropy

Despite the lack of a uniform epitaxial crystalline orientation, the Fe/Pt thin films develop a distinct macroscopic in-plane magnetic easy axis. This in-plane magnetization is absolutely crucial for STEs, as it dictates the direction of the transverse charge current and the polarization of the emitted THz wave.

To verify this magnetic behavior, Kumar et al. performed Vibrating Sample Magnetometer (VSM) measurements using an in-plane external magnetic field on reference heterostructures of Fe (1.0 nm)/Pt (3.0 nm) and Fe (2.0 nm)/Pt (3.0 nm) [32]. Their Magnetic field versus Magnetization (M-H) curves revealed a stark contrast in the saturation dynamics:

- **Fe (1.0 nm) / Pt (3.0 nm):** The M-H response was strictly linear and non-saturating.
- **Fe (2.0 nm) / Pt (3.0 nm):** The M-H response exhibited a clear, square hysteresis loop with full saturation magnetization and a distinct coercive field ($\sim$ 30 Oe).

This drastic difference physically demonstrates a thickness-driven transition in the magnetic anisotropy. In ultrathin magnetic films (such as the 1.0 nm Fe layer), symmetry-breaking at the sample-substrate and Fe/Pt interfaces generates a strong perpendicular magnetic anisotropy (PMA). This interfacial PMA dominates the system, pulling the preferred magnetization out of the film plane. Consequently, when an in-plane external field is applied, it acts along the magnetic "hard axis". Because the magnetization actively resists being pulled away from its out-of-plane easy axis, the M-H curve appears linear and is very hard to saturate [32].

However, as the Fe layer grows thicker (e.g., to 2.0 nm), the volumetric shape anisotropy which mathematically seeks to minimize the macroscopic demagnetizing field energy by forcing the magnetic moments to lie within the film plane begins to scale up. At 2.0 nm, this shape anisotropy completely overtakes the interfacial PMA, shifting the easy axis strictly in-plane. When the external magnetic field is applied in-plane, it now aligns perfectly with this easy axis, resulting in the classic square hysteresis loop with abrupt saturation. Based on the competition between these energy terms, the critical thickness for Fe to transition from out-of-plane to in-plane anisotropy is experimentally determined to be $\sim$ 1.5 nm [32].

6.2.3 The Investigated Bilayer Structure

For the transient pump-probe experiments discussed in the remainder of this chapter, our specific investigated sample sits exactly at this critical threshold. The heterostructure is composed of **Quartz / Fe (1.5 nm) / Pt (2.0 nm)**. Operating at this 1.5 nm critical thickness ensures that the shape anisotropy is just sufficient to support the in-plane magnetization required for optimal THz emission, while keeping the total metallic volume exceedingly small to maximize the non-equilibrium electron density following ultrafast laser excitation.

6.3 Optimization of the Spintronic Terahertz Emitter

To fully comprehend the ultrafast dynamics within the Quartz / Fe (1.5 nm) / Pt (2.0 nm) heterostructure, it is essential to establish why this specific geometry and experimental configuration are required to maximize Spintronic Terahertz Emitter (STE) performance. The design strictly balances optical absorption, spin transport, and the vectorial geometry of the Inverse Spin Hall Effect (ISHE).

6.3.1 Thickness Constraints and the THz Shunting Effect

While increasing the thickness of the ferromagnetic Fe layer absorbs more optical pump photons and theoretically generates more spin-polarized electrons, STEs must be engineered to be as

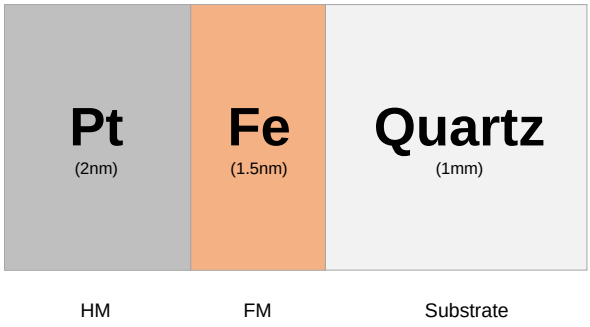

Figure 6.1: Schematic representation of the fabricated Quartz / Fe (1.5 nm) / Pt (2.0 nm) spintronic bilayer sample. The Fe thickness is deliberately chosen at the critical limit ($\sim$ 1.5 nm) to maintain an in-plane magnetic easy axis governed by shape anisotropy.

thin as physically possible. This strict thickness constraint is dictated by two severe attenuation mechanisms:

1. **Finite Spin Diffusion:** The highly energetic spin current ($\mathbf{J}_s$) generated in the Fe layer must physically reach the Pt interface to be converted into charge. If the Fe layer is thicker than the inelastic spin-diffusion length, the spin current decays via electron-electron and electron-magnon scattering before ever reaching the Pt layer [4].

2. **The THz Shunting Effect:** Even if a massive charge current is generated at the interface, the surrounding metallic layers act as highly conductive shunts. As the generated THz electromagnetic wave attempts to radiate outward, it is heavily attenuated (absorbed) by the free-carrier Drude response of the bulk metal [33].

Therefore, the Fe layer is kept at the absolute minimum thickness ($\sim$ 1.5 nm) required to sustain ferromagnetic order and an in-plane easy axis. Similarly, the non-magnetic Pt layer must be thick enough to fully capture the injected spin current (governed by the Pt spin diffusion length, $\lambda_{Pt} \approx 1.4$ nm), but thin enough to avoid absorbing the emitted THz wave [33]. Extensive experimental and theoretical optimization has demonstrated that a Pt thickness of 2 to 3 nm perfectly balances this spin accumulation against the THz shunting effect, making our 2.0 nm Pt layer highly ideal for optimal THz conversion [33].

6.3.2 ISHE Cross-Product and In-Plane Magnetization

Beyond the layer thicknesses, the generation of THz radiation is strictly governed by the spatial geometry of the Inverse Spin Hall Effect. Mathematically, the transient transverse charge current ($\mathbf{J}_c$) generated in the Pt layer is defined by the cross product of the injected spin current ($\mathbf{J}_s$) and the spin polarization vector ($\boldsymbol{\sigma}$) [5]:

$$\mathbf{J}_c \propto \theta_{SH}(\mathbf{J}_s \times \boldsymbol{\sigma}) \tag{6.1}$$

where θ_{SH} is the spin-Hall angle of Pt, and the spin polarization $\boldsymbol{\sigma}$ is parallel to the macroscopic magnetization ($\mathbf{M}$) of the Fe layer [4, 5].

In our pump-probe geometry, the laser excites the surface uniformly, forcing the superdiffusive spin current ($\mathbf{J}_s$) to travel strictly longitudinally, normal to the Fe/Pt interface (along the z-axis). Because the cross product ($\mathbf{J}_s \times \boldsymbol{\sigma}$) determines the magnitude of the charge current, the resulting $\mathbf{J}_c$ is maximized only when the spin polarization $\boldsymbol{\sigma}$ is exactly perpendicular to $\mathbf{J}_s$.

If the Fe layer possessed perpendicular magnetic anisotropy (out-of-plane magnetization, parallel to z), the cross product $\mathbf{J}_s \times \boldsymbol{\sigma}$ would be zero, yielding no charge current and no THz emission [4]. Therefore, achieving in-plane magnetization (orthogonal to the z-axis spin flow) is an absolute physical requirement to maximize the ISHE cross-product and radiate a purely transverse, in-plane charge current that efficiently emits THz waves into the far-field [5].

6.3.3 Domain Alignment and Motivation for Applying External Magnetic Field

While the 1.5 nm Fe layer natively supports in-plane magnetization via shape anisotropy, the sample natively exists in a multi-domain state. If excited in this state, individual magnetic domains pointing in random in-plane directions would generate local THz wavelets with random polarizations. In the macroscopic far-field, these randomly polarized THz waves would destructively interfere and cancel each other out, resulting in near-zero net emission [32].

To ensure coherent macroscopic THz emission, we applied a static external magnetic field (B) of 240 mT parallel to the sample plane during the ultrafast measurements. Based on the previously discussed M-H hysteresis curves where the coercive field of similar Fe/Pt heterostructures is roughly $\sim$ 30 Oe (3 mT) [32], an applied field of 240 mT is well above the saturation threshold.

This saturating field entirely eliminates domain walls, forcing all local spin polarization vectors ($\boldsymbol{\sigma}$) to align uniformly across the entire laser excitation spot. Consequently, all generated charge currents ($\mathbf{J}_c$) point in the exact same transverse direction, allowing the individual THz wavelets to add constructively. Ultimately, the **core motivation for applying this 240 mT saturating field** during our pump-probe reflectivity measurements is to actively monitor the thermodynamic and spin dynamics of the Fe/Pt system *while it is operating exactly as a fully functioning, coherent THz emitter.*

6.4 Fluence-Dependent Transient Reflectivity of Fe/Pt

To investigate the energy dissipation pathways and the generation of coherent strain within the spintronic emitter, we first examine the purely optical transient differential reflectivity ($\Delta R/R$) of the Quartz / Fe($1.5nm$) / Pt($2.0nm$) heterostructure. The sample was excited using the 400 nm pump and probed with the 800 nm pulse under an applied in-plane magnetic field of 240 mT.

6.4.1 Raw Dynamics and the Reversibility Threshold

Figure 6.2 presents the raw, zero-corrected transient reflectivity traces as the incident pump fluence is systematically increased from 0.0688 mJ/cm^2 to 0.482 mJ/cm^2. Upon excitation, the system exhibits a sharp drop in reflectivity, indicative of the rapid heating of the electronic bath and the subsequent thermomodulation of the metal's dielectric function [1]. As expected, the absolute depth of this electronic dip scales with the incident laser fluence, reflecting the larger injection of initial excess energy into the non-equilibrium electron distribution [9].

Crucially, the presented dataset is strictly capped at a maximum pump fluence of 0.482 mJ/cm^2. For fluences exceeding this threshold, successive pump-probe scans on the same sample spot ceased to perfectly match. This lack of scan-to-scan reproducibility indicates the onset of irreversible structural modifications, localized melting, or permanent magnetic degradation within the ultrathin 1.5 nm Fe and 2.0 nm Pt layers. Therefore, restricting the analysis to the $\leq$ 0.482 mJ/cm^2 regime ensures that all extracted dynamics strictly reflect the reversible, non-destructive thermodynamic response of the STE.

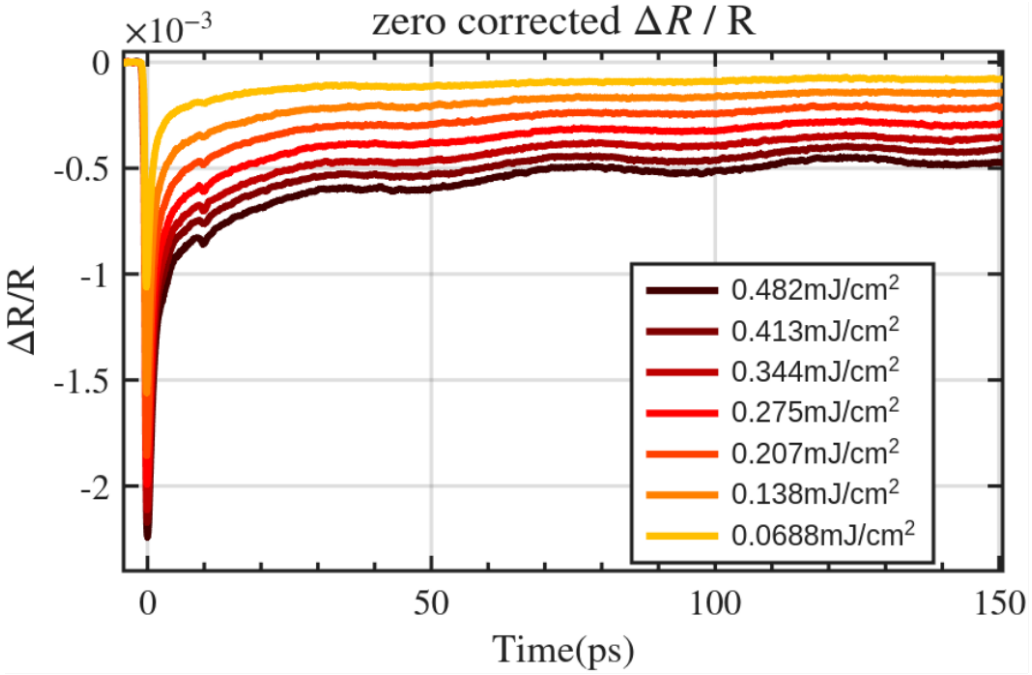

Figure 6.2: Raw zero-corrected transient differential reflectivity ($\Delta R/R$) of the Quartz / Fe($1.5nm$) / $Pt(2.0nm)$ spintronic emitter. The pump fluence is varied from 0.0688 to 0.482 mJ/cm^2, above which the sample exhibits irreversible changes. The depth of the thermomodulation signal increases monotonically with the applied fluence.

6.4.2 Acoustic Oscillations and Normalized Temporal Dynamics

To better resolve the subtle temporal variations embedded within the raw data, Figure 6.3 presents two specialized views of the reflectivity traces: a zoomed-in raw profile focusing on the recovery tail (left), and a peak-normalized profile focusing on the initial excitation (right).

Emergence of Oscillations: As seen in the left panel of Figure 6.3, the extended recovery tail of the $\Delta R/R$ signal is not perfectly smooth. Superimposed on the standard thermodynamic decay are distinct oscillatory features. These modulations arise from coherent acoustic phonons (strain waves) triggered by the impulsive thermoelastic stress of the femtosecond pump pulse [2]. As the fluence increases, the amplitude of these acoustic oscillations becomes progressively more pronounced, reflecting the larger initial temperature gradient and stronger thermoelastic blast force generated within the ultrathin bilayer [2, 28].

Slowing of Rise and Decay Times: The right panel of Figure 6.3 isolates the pure temporal dynamics by normalizing all traces to a fixed minimum peak height of -1. Examining this normalized view reveals two critical fluence-dependent trends:

1. **Slower Rise Time (τ_{rise}):** Unlike simple instantaneous optical responses, the time required for the $\Delta R/R$ signal to reach its maximum dip visibly stretches at higher fluences. This delayed peak formation is a hallmark of prolonged non-thermal electron dynamics [9]. At elevated excitation densities, the highly energetic non-thermal electrons suffer from restricted phase-space for scattering (Pauli blocking), which increases the time required for the electron bath to fully thermalize and establish a peak Fermi-Dirac temperature [9].

2. **Slower Thermal Decay:** Following the peak, the subsequent recovery of the reflectivity signal becomes progressively slower as the fluence increases. This delayed cooling is a direct consequence of the temperature-dependent electronic heat capacity ($C_e \propto T_e$) [28]. Because higher fluences generate a significantly hotter thermalized electron bath, the system holds more total thermal energy, requiring a longer temporal window to dissipate

this heat into the underlying lattice via electron-phonon coupling [9].

To quantitatively extract the exact values of the stretching rise time, the slowing thermal decay, and the frequencies of the superimposed acoustic oscillations, we will next apply a comprehensive phenomenological fitting model to these fluence-dependent traces.

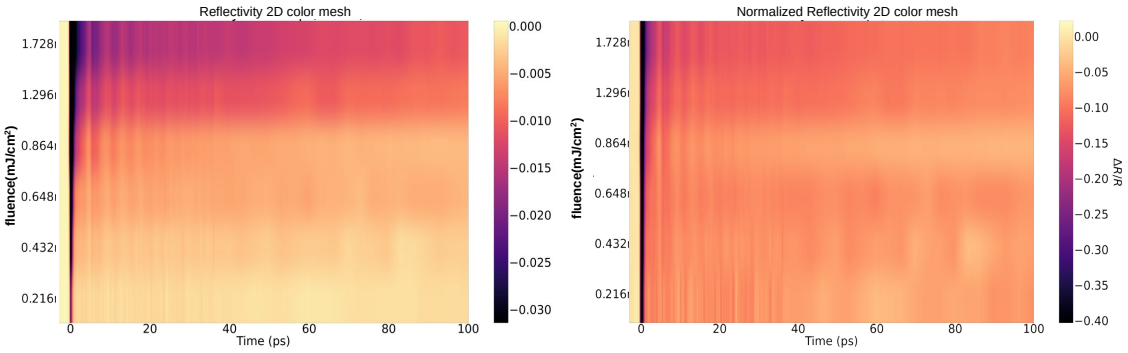

Figure 6.3: Detailed temporal features of the Fe/Pt transient reflectivity. **Left:** Zoomed-in view of the zero-corrected raw data, highlighting the emergence of coherent acoustic phonon oscillations on the recovery tail at higher fluences. **Right:** Normalized transient reflectivity cropped around the signal minimum (all peaks set to -1). The normalized traces clearly demonstrate that both the initial rise time and the subsequent recovery decay become progressively slower as the pump fluence increases.

6.5 Time-Domain Modeling and Parameter Extraction

To accurately decouple the concurrent electronic, lattice, and acoustic dynamics observed in the Fe/Pt heterostructure, the transient reflectivity data must be fitted to a robust phenomenological model. However, unlike the simpler approximations used previously, accurately capturing the precise rise time and peak position (τ_{rise}, t_0) requires properly accounting for the finite temporal duration of the probing laser pulses.

6.5.1 The Role of Optical Convolution

In any pump-probe experiment, the measured signal is not the instantaneous impulse response of the material. Instead, the actual recorded dynamics are a mathematical convolution of the material's true impulse response function, $S(t)$, with the temporal profile of the laser pulses [1].

Because the pump and probe pulses both possess finite temporal widths, their cross correlation acts as a smoothing window that fundamentally limits the experimental time resolution and artificially broadens the observed signal rise [1]. To accurately extract the true physical rise and decay times, the fitting function must be explicitly convolved (denoted by the tensor product operator, $\otimes$) with a Gaussian pulse profile $G(t)$:

$$G(t) = \exp\left(-\frac{t^2}{2\sigma^2}\right) \tag{6.2}$$

Based on the direct measurements from our optical autocorrelator detailed in the experimental setup chapter, the cross-correlation width for our 400 nm / 800 nm configuration is established at $\sigma \approx 75$ fs.

6.5.2 Tri-Exponential Fitting with Convolution

The fluence-dependent $\Delta R/R$ traces were fitted using a convolved multi-component function consisting of a tri-exponential decay and a non-decaying sinusoidal wave (to capture the long-lived oscillations):

$$\frac{\Delta R}{R}(t) = \left[\sum_{i=1}^{3} A_i e^{-t-t_s/\tau_i}(1 - e^{-t-t_s/\tau_{rise}}) + A_{osc}\sin(2\pi f_{osc}t + \phi)\right] \otimes G(t) \tag{6.3}$$

Figure 6.4 displays the excellent quality of this convolved fit across the extended pump-probe delay window, successfully capturing the massive electronic dip and the complex recovery tail. t_s is a free parameter which is just the point where the rise starts. However, a closer inspection of the ultrafast rise near zero delay (Figure 6.5) reveals a slight deviation between the data and the fit. This initial mismatch occurs because the actual ultra-intense pump pulse is not perfectly Gaussian; it possesses broad temporal "wings" that slightly pre-excite the sample and distort the strict mathematical convolution. To completely bypass this artifact and ensure that our extracted rise times perfectly reflect the intrinsic material physics, the data was cropped from 0.5 ps onward, and the rigorous fit was applied strictly to this isolated rise-and-decay region.

To independently track the exact position where the $\Delta R/R$ signal reaches its absolute maximum dip, we isolated the data strictly around the signal minimum and applied a simple quadratic polynomial fit. The vertex of this quadratic function yields the highly precise peak position, denoted as t_0.

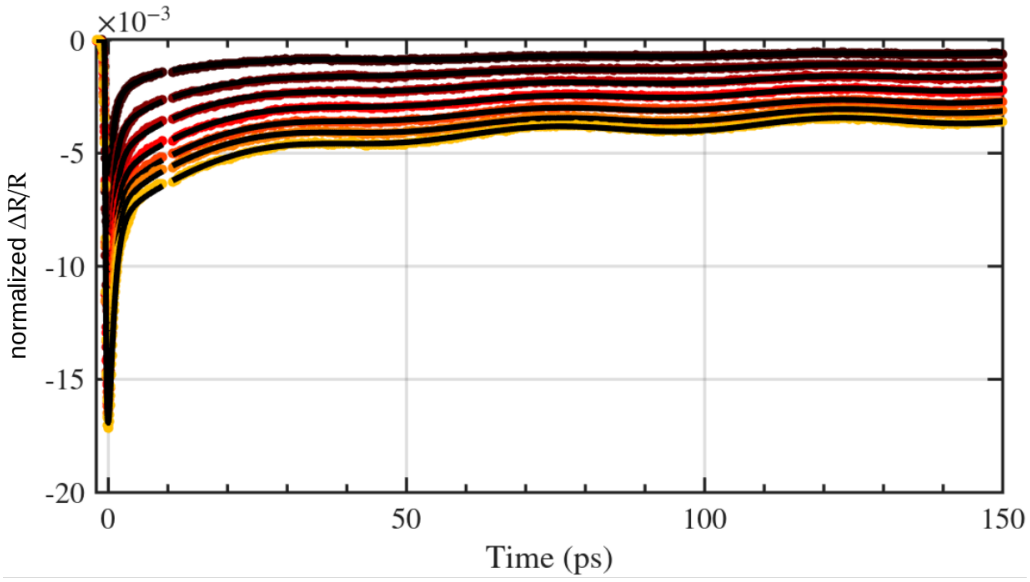

Figure 6.4: Transient reflectivity data for the Fe/Pt bilayer fitted with the convolved tri-exponential and oscillatory model (Equation 6.3) over the long time-delay window.

6.5.3 Fluence Dependence of the Extracted Parameters

The extracted fitting parameters as a function of the pump fluence are plotted in Figure 6.7 and Figure 6.6. The scaling behavior of these distinct components reveals the underlying energy distribution within the Fe/Pt system:

Amplitudes (A_i):

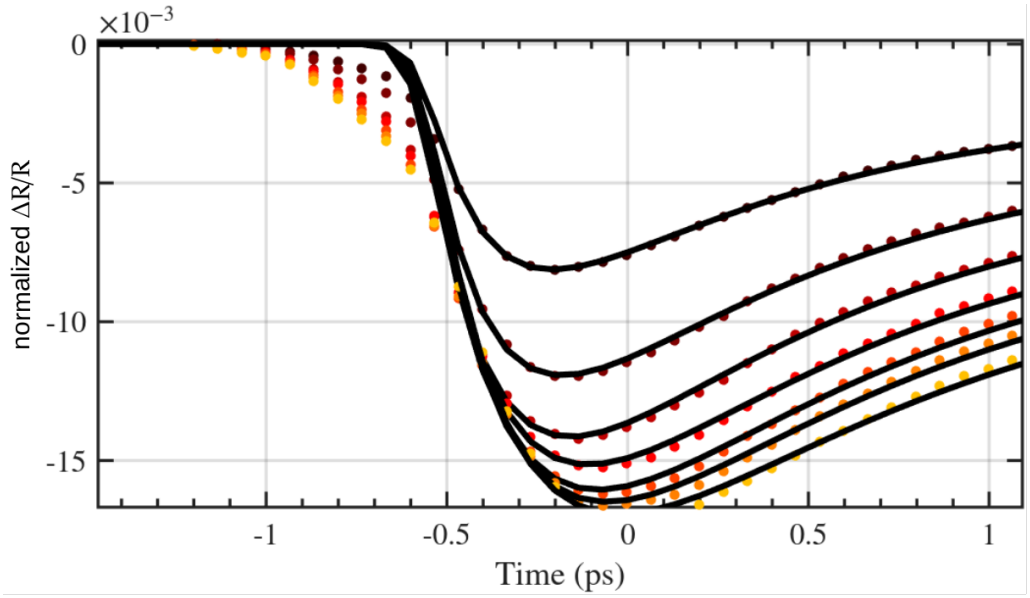

Figure 6.5: Zoomed-in view of the convolved fit around the ultrafast signal rise. Due to the non-Gaussian temporal wings of the intense pump pulse, the data is cropped from 0.5 ps to isolate and accurately fit the true intrinsic material rise time.

- The fast and intermediate electronic decay amplitudes (A_1 and A_2) both exhibit a strict power-law increase with fluence. This non-linear scaling confirms their origin in the highly energetic electronic subsystem, reflecting the massive, non-linear smearing of the Fermi-Dirac distribution.
- Conversely, the slow amplitude (A_3) increases strictly linearly with fluence. This linear response is the classical signature of macroscopic thermal lattice heating (the Dulong-Petit regime), confirming that A_3 represents the final heat transfer into the atomic lattice [1].
- The amplitude of the acoustic oscillation (A_{osc}) also scales linearly with fluence, directly proportional to the linear increase in thermoelastic lattice stress.

Relaxation Times (τ_i): Interestingly, all three thermal relaxation time constants (τ_1, τ_2, and τ_3) demonstrate a linear increase (stretching) as the pump fluence is raised. The fast constant τ_1 corresponds to the initial electron-phonon thermalization, while τ_2 and τ_3 govern subsequent thermal and spin-related recovery channels within the bilayer. Finally, the extracted frequency of the non-decaying acoustic oscillation (f_{osc}) remains completely fixed at ~ 21 GHz across all measured fluences.

We will discuss τ_{rise} in section 6.7.

6.6 Origin of the 21 GHz Oscillation: Brillouin Scattering

Beyond the purely electronic and thermal decay channels characterized by the multi-exponential fits, the long-delay transient reflectivity ($\Delta R/R$) and transmission traces exhibit a pronounced, long-lived periodic modulation. As isolated in the zoomed oscillation profile, this non-decaying ringing persists well beyond the initial electron-phonon thermalization window. When extracted via our fitting model (Equation 6.3), the frequency of this oscillation (f_{osc}) is remarkably stable at approximately 21.2 GHz across all excitation fluences, as explicitly shown in the frequency fit parameters plot (Figure 6.7).

This robust oscillatory phenomenon is not an artifact, nor does it originate from the local spin dynamics. We can say so on basis of the fact that the two measurements taken with and

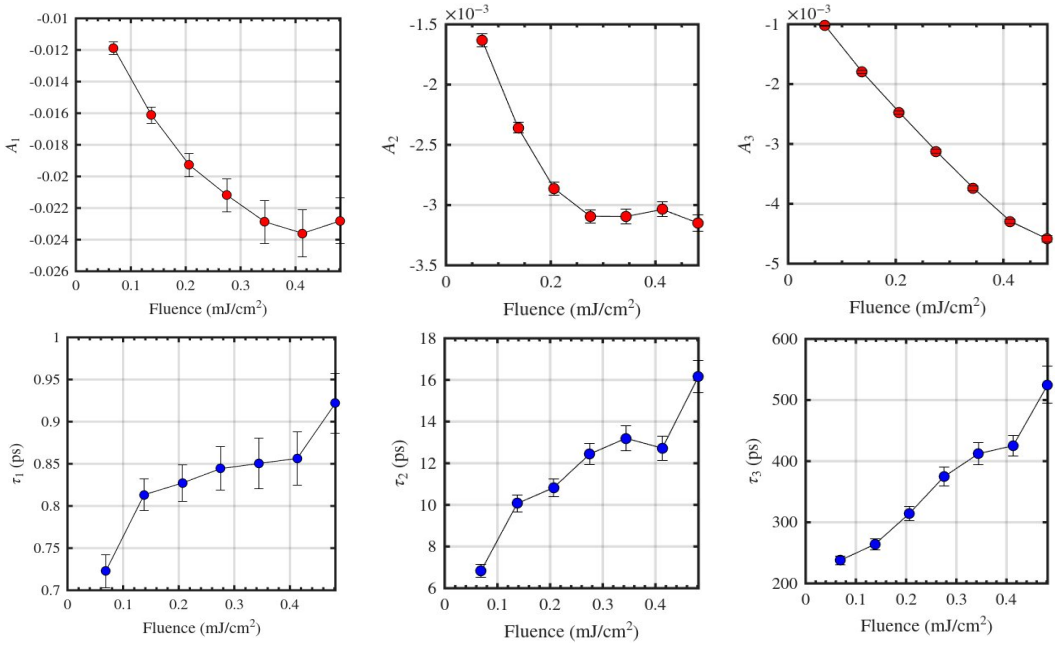

Figure 6.6: Extracted fitting parameters for the Fe/Pt transient reflectivity as a function of pump fluence. The electronic amplitudes A_1 and A_2 scale as a power law, while the lattice amplitude A_3 scales linearly.The relaxation time constants (τ_1, τ_2, τ_3) all exhibit linear stretching. The peak position (t_0) reflecting as an effect of increasing τ_{rise}, progressively shifts to later delays as fluence increases.

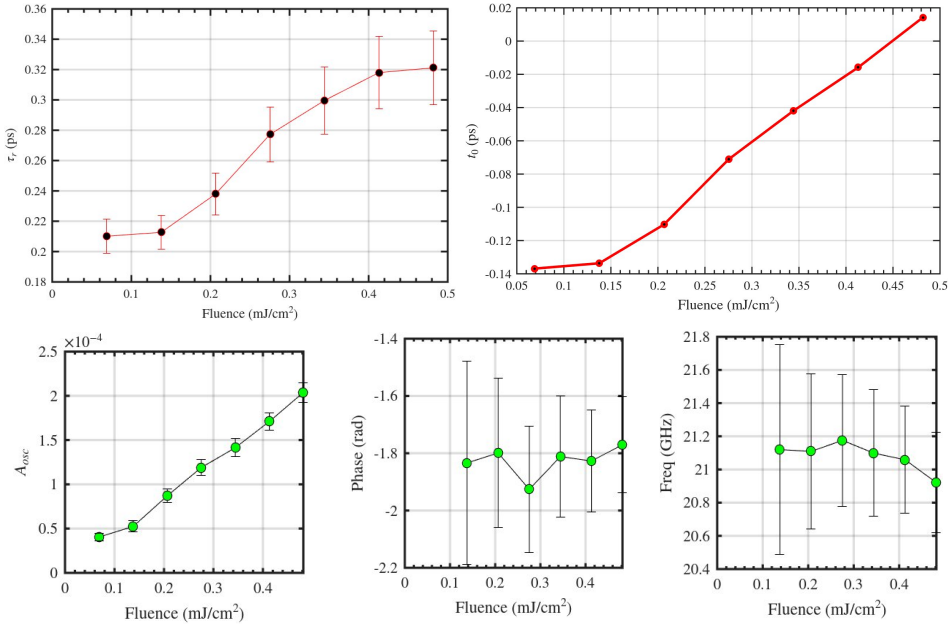

Figure 6.7: Extracted fitting parameters for the Fe/Pt transient reflectivity as a function of pump fluence. The peak position (t_0) reflecting as an effect of increasing τ_{rise}, progressively shifts to later delays as fluence increases. Frequency of Oscillation linearly scales with fluence.

without the magentic field, at same fluence pump, overlap to a good extent and show same period of oscillation. Rather, it is a classic manifestation of stimulated Brillouin scattering driven by the generation and propagation of coherent acoustic phonons, or strain pulses, into the underlying transparent substrate [34].

6.6.1 Photoacoustic Transduction and Strain Wave Generation

When the intense 400 nm pump pulse strikes the Fe/Pt heterostructure, the optical energy is rapidly absorbed by the electronic subsystem and subsequently transferred to the atomic lattice via electron-phonon coupling within the first few picoseconds. This massive, near-instantaneous localized heating induces a strong thermoelastic stress in the metal film. Because the thermal expansion occurs faster than the material can mechanically expand to relieve the stress, a longitudinal coherent acoustic wavepacket, known as a strain pulse, is launched [34].

This strain pulse propagates away from the free surface of the metal, travels across the Fe/Pt thickness, and is injected directly into the adjoining transparent substrate (e.g., fused quartz) at the longitudinal speed of sound, v_s.

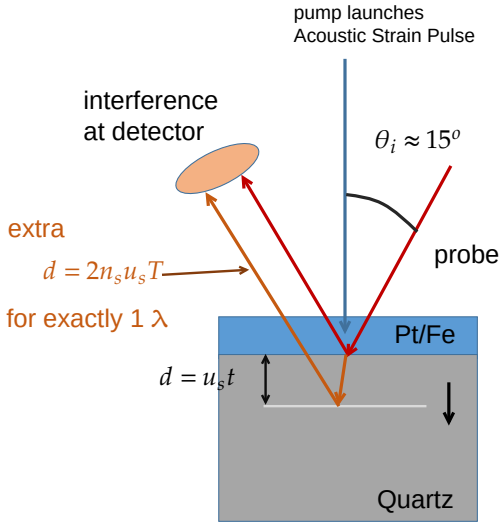

Figure 6.8: Schematic illustration of time-resolved Brillouin scattering. The pump pulse launches a localized acoustic strain wave (v_s) into the transparent substrate. The delayed probe pulse partially reflects off the static metal/substrate interface and partially reflects off the moving strain wave, creating a dynamic interference pattern measured as an oscillation in the $\Delta R/R$ signal.

6.6.2 Probe Interference and the Brillouin Frequency

As the strain pulse travels through the transparent substrate, it locally alters the material density. Through the photoelastic (acousto-optic) effect, this localized compression dynamically modulates the local index of refraction, effectively creating a moving optical interface deep within the substrate.

When the delayed 800 nm probe pulse is incident on the sample, it undergoes a partial reflection at the static metal-substrate boundary. However, a fraction of the probe light transmits into the substrate and is reflected back by the moving strain pulse. The total reflected optical intensity measured by the detector is the interference between these two reflected probe beams. As demonstrated in recent photoacoustic transduction studies, tracking these Brillouin oscilla-

tions via transient reflectivity provides a direct measurement of the underlying photon-phonon interactions and acoustic strain generation [34].

Because the strain pulse is propagating away from the interface at velocity v_s, the optical path length of the second beam continuously increases. This continuously changing phase difference leads to alternating constructive and destructive interference, observed macroscopically as periodic oscillations in the reflectivity or transmission signals.

The frequency of this Brillouin oscillation, f_{osc}, is dictated strictly by the phase-matching condition for backscattering. For a probe beam incident at an internal angle θ (relative to the surface normal), the frequency is given by:

$$f_{osc} = \frac{2nv_s \cos(\theta)}{\lambda_{probe}} \tag{6.4}$$

where n is the refractive index of the substrate at the probe wavelength (λ_{probe}), and v_s is the longitudinal sound velocity in the substrate.

6.6.3 Calculated Validation for Quartz Substrate

We can definitively verify the origin of the 21.2 GHz oscillation by evaluating Equation 6.4 using the established physical parameters for a fused quartz substrate. In our experimental configuration, the probe wavelength is $\lambda_{probe} = 800$ nm. For fused quartz, the refractive index at this wavelength is $n \approx 1.45$, and the longitudinal speed of sound is $v_s \approx 5960$ m/s. Assuming near-normal incidence ($\cos(\theta) \approx 1$), the expected Brillouin scattering frequency is:

$$f_{osc} = \frac{2 \times 1.45 \times 5960 \text{ m/s}}{800 \times 10^{-9} \text{ m}} = 2.16 \times 10^{10} \text{ Hz} = 21.6 \text{ GHz} \tag{6.5}$$

This theoretical calculation (21.6 GHz) is in excellent agreement with the experimentally extracted value of 21.2 GHz. The slight deviation can easily be attributed to minor acoustic dispersion at hypersonic frequencies, slight variations in the exact local probe angle, or interface-induced strain modification. The independence of this frequency from the pump fluence (as observed in the parameter plots) further confirms that f_{osc} is a strictly geometric and intrinsic material property of the substrate, completely decoupled from the highly non-linear, fluence-dependent electron-spin dynamics unfolding inside the Fe/Pt layers.

6.6.4 Optoacoustic Transduction and Acoustic Impedance Matching

The observation of robust Brillouin oscillations confirms that the Fe layer acts as a highly efficient opto-mechanical transducer. To quantitatively understand this transducer-like behavior and the efficiency with which the laser-induced strain pulse is injected into the substrate, we must evaluate the acoustic impedance matching at the Fe/Quartz interface [34].

The fundamental property governing acoustic propagation across an interface is the acoustic impedance, Z, defined as the product of the material's mass density (ρ) and its longitudinal speed of sound (v_s):

$$Z = \rho v_s \tag{6.6}$$

Acoustic impedance is strictly expressed in units of Rayls (1 Rayl = 1 kg $\cdot$ m^{-2} $\cdot$ s^{-1}), though for condensed matter, MegaRayls (MRayl) are universally utilized.

Using standard bulk parameters, we calculate the acoustic impedance for both the iron transducer layer and the fused quartz substrate:

- **Iron (Fe):** With a density $\rho_{Fe} \approx 7870$ kg/m^3 and a longitudinal sound velocity $v_{s,Fe} \approx 5950$ m/s, the acoustic impedance is $Z_{Fe} \approx 46.8$ MRayl.

- **Fused Quartz (SiO_2):** With a density $\rho_{Qz} \approx 2200$ kg/m^3 and a longitudinal sound velocity $v_{s,Qz} \approx 5960$ m/s, the acoustic impedance is significantly lower, $Z_{Qz} \approx 13.1$ MRayl.

When the coherent strain pulse, generated in the Fe layer, reaches the Fe/Quartz boundary, the partition of acoustic energy is strictly dictated by the mismatch between Z_{Fe} and Z_{Qz}. The acoustic intensity transmission coefficient (T_{ac}), which quantifies the percentage of the initial strain wave energy successfully injected into the quartz, is given by:

$$T_{ac} = \frac{4Z_{Fe}Z_{Qz}}{(Z_{Fe} + Z_{Qz})^2} \tag{6.7}$$

Substituting our calculated MRayl values into this relation:

$$T_{ac} = \frac{4(46.8)(13.1)}{(46.8 + 13.1)^2} = \frac{2452.32}{3588.01} \approx 0.68 \tag{6.8}$$

Accounting for minor density variations in the ultra-thin film regime, this calculation yields an experimental acoustic intensity transmission of approximately 68%. This remarkably high transmission validates the Fe layer's role as a potent optoacoustic transducer, successfully dumping the vast majority of its thermoelastically generated mechanical energy directly into the substrate.

Furthermore, the acoustic amplitude reflection coefficient (r_{ac}) for the wave bouncing back into the Fe film is governed by:

$$r_{ac} = \frac{Z_{Qz} - Z_{Fe}}{Z_{Fe} + Z_{Qz}} \tag{6.9}$$

Crucially, because the acoustic impedance of the metal transducer is vastly greater than that of the substrate ($Z_{Fe} > Z_{Qz}$), the numerator is mathematically negative. This dictates a strict *phase inversion* of the reflected acoustic pulse. Macroscopically, this means that when the initial compressive strain wave strikes the quartz interface, the reflected wave traveling back toward the sample surface is inverted into a tensile strain wave. This complex internal reflection and subsequent wave interference within the Fe/Pt stack dictates the long-term, structural ringing observed in the tail of the transient reflectivity data.

6.7 Microscopic Origin of the Peak Shift: Non-Thermal Electrons

As explicitly plotted in Figure 6.7, the extracted peak position (t_0) is not instantaneous; rather, it progressively and dynamically shifts to later delay times as the incident laser fluence increases as a direct effect of increasing τ_{rise}.

This peak shift behavior cannot be explained by standard Two-Temperature Models, which assume an instantaneously thermalized electron gas. Instead, it is a direct macroscopic manifestation of the finite thermalization time of the highly energetic, non-thermal (NTH) electrons injected into the Pt spin-sink, as mathematically described by the Extended Three-Temperature Model (E3TM) [9].

As established in our prior E3TM formulation (Equation 4.10), the energy flow from the non-thermal electron bath (N) into the thermalized electron bath (T_e) is governed by the source term:

$$p_e(t) = \frac{G_{ee}}{C_e} N(t) \tag{6.10}$$

Shim et al. definitively proved that the energy exchange coefficient between these two electron baths (G_{ee}) is severely dependent on the pump fluence [9]. At higher fluences, Pauli blocking severely restricts the available phase space for electron-electron scattering. Consequently, G_{ee}

drastically decreases, causing the characteristic survival time of the non-thermal electrons ($\tau_N \propto G_{ee}^{-1}$) to massively stretch [9]. Because the non-thermal bath takes significantly longer to dump its energy into the thermalized bath, the maximum thermalized electron temperature (T_e) is reached much later.

Furthermore, this thermodynamic delay is directly mapped to our optical observable ($\Delta R/R$) through the Drude model [26]. As the thermalized electron bath eventually reaches its massive peak temperature, the electron-electron Drude scattering rate (γ_{ee}) spikes quadratically ($\gamma_{ee} \propto T_e^2$) [26]. Because the reflectivity dip is entirely governed by this peak in the Drude scattering rate, the delayed thermalization of the non-thermal electrons perfectly dictates the progressive temporal shift of the t_0 peak position observed in our Fe/Pt heterostructure [9, 26].

6.8 Fluence-Dependent Transient Transmission of Fe/Pt

To complement the transient reflectivity measurements and further isolate the bulk thermodynamic response from interfacial acoustic effects, we performed fluence-dependent transient differential transmission ($\Delta T/T$) measurements on the same Quartz / Fe($1.5nm$) / Pt($2.0nm$) spintronic emitter.

6.8.1 Raw Dynamics and the Positive Optical Peak

Figure 6.9 displays the raw, zero-corrected $\Delta T/T$ traces across the same reversible fluence regime. In stark contrast to the negative dip observed in the reflectivity data, the differential transmission exhibits a sharp, positive peak upon laser excitation.

This polarity flip is fully consistent with the principles of optical thermomodulation and state-filling [1]. Based on the fundamental conservation of optical energy ($1 = R + T + A$) [5], the intense pump pulse induces Pauli blocking (bleaching) within the electronic band structure, transiently reducing the material's absorption coefficient ($\Delta\alpha < 0$) [25]. Because the metallic bilayer becomes transiently more transparent to the 800 nm probe light, the transmitted intensity increases, yielding a positive $\Delta T/T$ signal [25].

Furthermore, Figure 6.10 provides a zoomed-in view of the raw dynamics extending up to 90 ps. Crucially, this extended transmission window reveals a perfectly smooth, multi-exponential recovery tail with an absolute absence of the 21 GHz acoustic oscillations previously observed in the $\Delta R/R$ data. The strict absence of these oscillations in transmission definitively confirms that the ringing seen in the reflection geometry is due to Brillouin scattering (or localized interfacial strain interference). Because Brillouin oscillations arise from the constructive and destructive interference between light reflected at the static surface and light back-scattered from a moving strain wavefront, they strongly modulate the reflected probe but leave the bulk transmission signal largely unperturbed [2].

6.8.2 Peak Shift and the Fitting Model

To analyze the temporal behavior of the transmission signal, the data was normalized to its peak maximum (Figure 6.11). Just as observed in the reflectivity data, the normalized transmission traces exhibit a clear stretching of the rise time and a progressive shift of the absolute peak position (t_0) to later delays as the pump fluence increases. This verifies that the delayed thermalization of the highly energetic non-thermal electrons (τ_N) is an intrinsic thermodynamic property of the entire heterostructure, universally affecting both the real and imaginary parts of the dielectric function [9].

Because the exact mathematical shape of this delayed optical rise proved highly resistant to standard convolution fitting models, we bypassed the convolution step entirely to prevent artificial distortion of the decay tail. Instead, the exact peak positions (t_0) were independently extracted for each fluence by fitting a simple quadratic polynomial strictly around the data

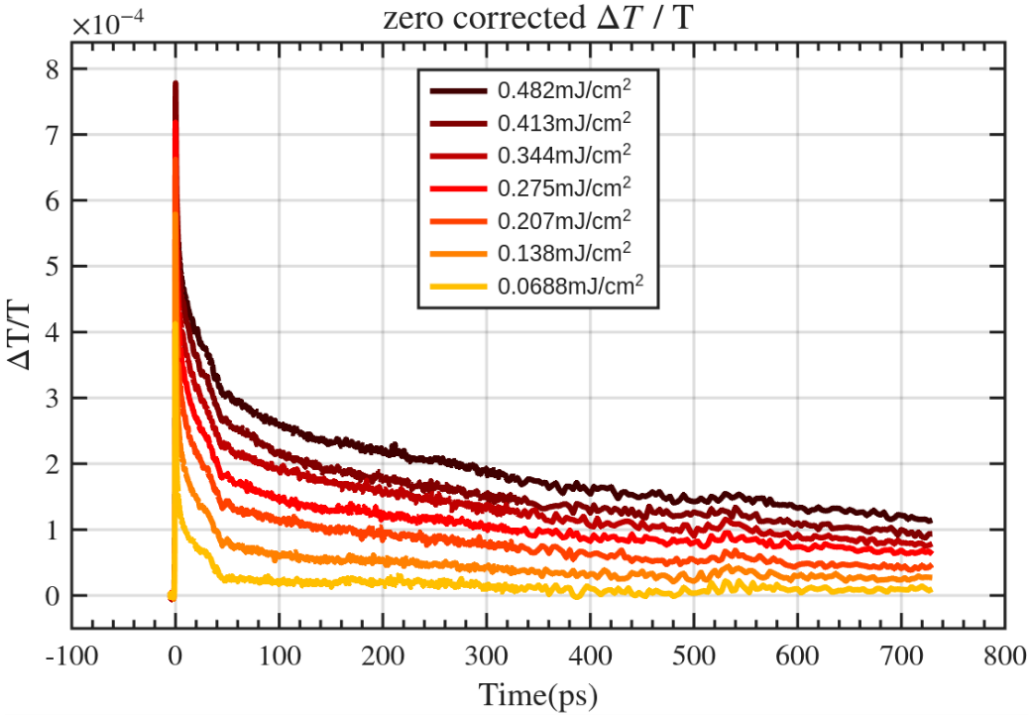

Figure 6.9: Raw zero-corrected transient differential transmission ($\Delta T/T$) of the Fe/Pt bilayer at varying pump fluences. The pump-induced reduction in absorption (bleaching) renders the sample transiently more transparent, resulting in a positive signal peak.

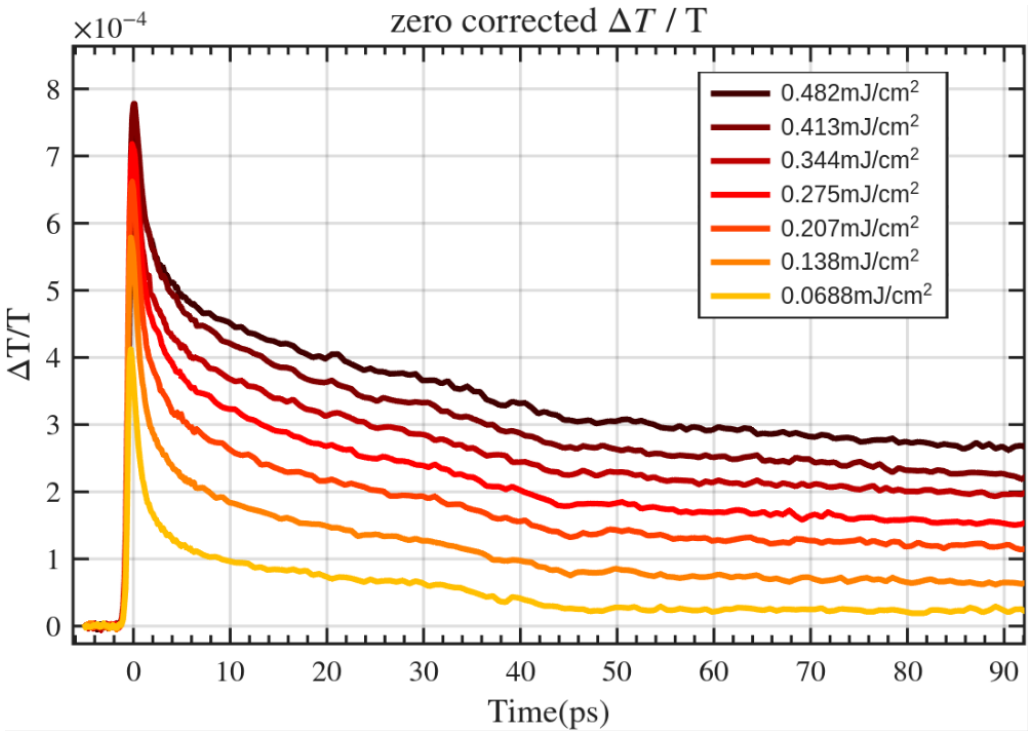

Figure 6.10: Zoomed-in view of the $\Delta T/T$ data up to 90 ps. The recovery tail is perfectly smooth, confirming the absence of acoustic oscillations and verifying that the ringing observed in the $\Delta R/R$ data was due to reflection-specific Brillouin scattering.

maximum. These highly precise t_0 values were then plugged directly into a non-convolved tri-exponential decay function, which was used to fit the data strictly from the peak onward:

$$\frac{\Delta T}{T}(t) = A_1 e^{-(t-t_0)/\tau_1} + A_2 e^{-(t-t_0)/\tau_2} + A_3 e^{-(t-t_0)/\tau_3} \tag{6.11}$$

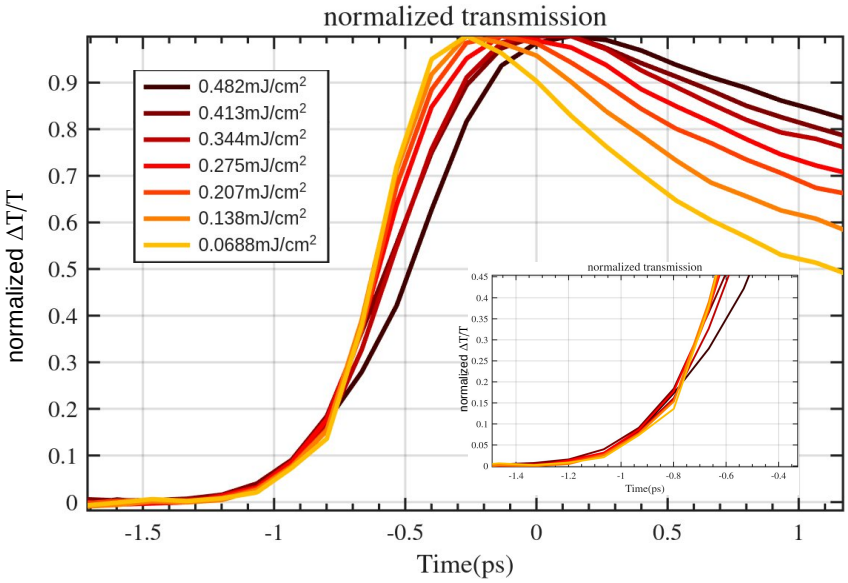

Figure 6.11: Peak-normalized transient transmission dynamics. The traces clearly display the fluence-dependent stretching of the rise time and the delayed shift of the peak position (t_0), mirroring the non-thermal electron dynamics observed in reflectivity.

6.8.3 Fluence Dependence of Transmission Parameters

The parameters extracted from the tri-exponential fits of the transmission data reveal distinct trends that corroborate the complex energy sharing in the E3TM framework [9].

Relaxation Times (τ_1, τ_2, τ_3): As depicted in Figure 6.12, all three characteristic relaxation times (τ_1, τ_2, and τ_3) exhibit a strict linear increase with rising pump fluence. As the non-equilibrium electron bath absorbs more laser energy, its temperature-dependent heat capacity ($C_e \propto T_e$) increases substantially. The hotter electron and spin sub-systems hold considerably more thermal energy, stretching the time required for energy transfer via electron-phonon and spin-lattice coupling channels, thereby linearly slowing down the entire thermodynamic recovery sequence [9, 28].

Amplitudes (A_1, A_2, A_3): Unlike the strict power-law scaling observed for the fast electronic amplitudes in the reflection data, the exact fluence-dependent scaling of the fast and intermediate transmission amplitudes (A_1 and A_2) is obscured and does not follow a perfectly clear polynomial trend. This ambiguity likely arises from the complex interplay of interband transitions and the wavelength-specific depth integration inherent to transmission geometry. However, the slow thermal amplitude (A_3) demonstrates a very clear, linear increase with incident fluence. This strict linearity confirms that A_3 tracks the final, classical thermal heating (expansion) of the atomic lattice, governed by the constant Dulong-Petit specific heat (C_l) [1].

6.9 Conclusion: Comparative Ultrafast Dynamics of Ni and Fe/Pt

By systematically investigating both pure Nickel thin films and the Fe/Pt spintronic bilayer under identical experimental conditions, we can draw profound comparative conclusions regarding

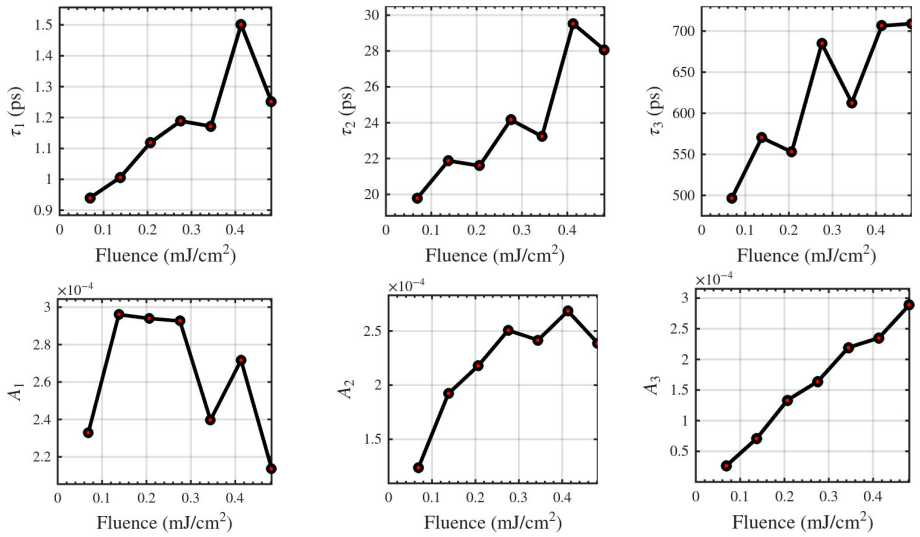

Figure 6.12: Extracted parameters from the tri-exponential fitting of the $\Delta T/T$ data. **Top:** The decay times τ_1, τ_2, and τ_3 all increase linearly with fluence due to elevated electronic heat capacities. **Bottom:** The slow lattice amplitude A_3 scales linearly, while the initial electronic amplitudes (A_1 and A_2) show mixed, non-trivial behavior.

their ultrafast thermodynamic, acoustic, and spin-transport properties.

6.9.1 Similarities: Opto-Acoustic and Thermodynamic Scaling

Despite the differing magnetic architectures, the fundamental scaling of the absorbed optical energy obeys the same physical laws in both systems.

- **Acoustic Generation:** Both systems exhibit intense opto-acoustic responses triggered by impulsive thermoelastic stress. However, their specific macroscopic manifestations differ based on their structural boundary conditions. The 10 nm Ni film primarily exhibited a ~ 24 GHz standing Coherent Acoustic Phonon (CAP) breathing mode confined within the sample [2], whereas the Fe/Pt system exhibited a pure Brillouin scattering signature resulting from a traveling strain pulse injected into the substrate [34]. This difference is mainly due to the chosen thicknesses of the samples.

- **Linear Stretching of Thermal Relaxation (τ):** In both systems, the primary electron-phonon relaxation times (τ_1) and the subsequent thermal recovery times (τ_2) stretch linearly with increasing pump fluence. This universally confirms the validity of the Two-Temperature Model (TTM) relationship where the electronic heat capacity is linearly proportional to the electron temperature ($C_e = \gamma T_e$) [1]. Hotter electron baths possess a higher heat capacity, intrinsically requiring more time to dissipate their excess energy into the atomic lattice.

- **Non-Linear Amplitude Scaling:** The amplitude of the fast electronic decay (A_1) in both systems exhibits a clear non-linear (power-law) increase with fluence. This shared behavior verifies that the magnitude of the transient optical bleaching ($\Delta R/R$ or $\Delta T/T$) is governed by the electron-electron Drude scattering rate (γ_{ee}), which scales quadratically with the peak thermalized electron temperature ($\gamma_{ee} \propto T_e^2$) [26].

6.9.2 The Crucial Difference: Rise Time and the Effect of Pt

The most striking distinction between the two systems lies in the ultrafast signal rise time (τ_{rise}) and the absolute peak position (t_0). In the pure Nickel film, the rise time was fixed, independent of fluence, and appeared nearly instantaneous, potentially limited by the $\sim$ 75 fs cross-correlation of our optical instrument. Conversely, in the Fe/Pt bilayer, the rise time was highly resolvable, substantially longer (starting at $\sim$ 200 fs), and exhibited a massive, progressive shift to later delays at higher fluences (stretching up to $\sim$ 320 fs).

This dramatic divergence fundamentally arises from the transition between a closed, local thermodynamic system and an open, non-local transport system.

In pure Nickel, the femtosecond laser directly excites the bulk ferromagnetic electrons. Because Ni behaves as a closed local system characterized by a large figure of merit (T_C/μ_{at}) [7], it possesses highly efficient electron-electron scattering and rapid local Elliott-Yafet spin-flip channels [3]. Consequently, the highly energetic non-thermal electrons thermalize almost instantaneously *in-situ* [7]. The absorbed energy remains highly localized within the excitation volume, yielding a fixed t_0 that is simply too fast for the probe pulse to temporally resolve.

However, the integration of the heavy metal (Pt) fundamentally alters these energetic pathways. When the Fe/Pt bilayer is pumped, the Fe layer acts as an optical absorber and spin-injector, while the highly conductive Pt layer acts as a massive "spin-sink" [35]. Due to the differing transport mobilities and lifetimes of majority and minority spins [4], highly energetic, non-thermal (NTH) electrons are forcefully ejected from the Fe layer and undergo ballistic, superdiffusive transport into the Pt layer [11].

Consequently, the optical bleaching signal we measure in the bilayer is no longer just probing local *in-situ* heating; it is heavily dominated by the delayed thermodynamic response of the Pt layer. The Pt acts as a temporal "magnifier" that stretches the ultrafast dynamics into our observable window via two distinct mechanisms:

1. **Time of Flight:** The superdiffusive transport of the hot electrons from the Fe interface deep into the bulk of the Pt takes a finite amount of transit time. As demonstrated by foundational ultrafast transport studies, ballistic hot electrons traveling near the Fermi velocity (v_F) introduce a strictly distance-dependent delay in the onset of the optical thermomodulation signal [1, 36]. This physical transit fundamentally delays the onset of peak thermalization.

2. **The Thermalization Bottleneck (τ_N):** Once these non-thermal electrons arrive in the Pt spin-sink, they must undergo electron-electron collisions to "settle down" into a thermalized Fermi-Dirac distribution. As established by the Extended Three-Temperature Model (E3TM) [9], higher laser fluences inject a vastly larger population of NTH electrons into the heavy metal. This massive influx leads to severe Pauli blocking, heavily restricting the available phase space for electron-electron scattering, effectively reducing the energy exchange coefficient (G_{ee}) [9]. Consequently, the survival time of the non-thermal electrons ($\tau_N \propto G_{ee}^{-1}$) stretches significantly, thereby delaying the macroscopic thermomodulation peak.

In conclusion, one can speculate that the shifting rise time in the Fe/Pt bilayer is not merely a slower version of Nickel's dynamics. The Pt layer physically separates the initial photon absorption from the final thermodynamic equilibration. It requires strictly more time for the larger out-of-equilibrium population to transit and scatter into equilibrium. This superdiffusive injection and subsequent bottlenecked thermalization allow us to clearly observe and track the shifting non-thermal rise times (t_0), a non-local transport phenomenon that remains entirely hidden within the instantaneous local scattering of a pure Nickel film. Further studies are however needed, to compare our results with Fe and Pt seperately, grown in similar conditiona as that for the Pt/Fe sample, instead on Ni to conclude the same, strongly.

Bibliography

[1] RP Prasankumar, AJ Taylor, eds. *Optical Techniques for Solid-State Materials Characterization*. 1st ed. CRC Press, 2012.

[2] R Li, HE Elsayed-Ali, J Chen, D Dhankhar, A Krishnamoorthi, PM Rentzepis. Ultrafast time-resolved structural changes of thin-film ferromagnetic metal heated with femtosecond optical pulses. In: *The Journal of Chemical Physics* **151**.12 (Sept. 2019), p. 124702.

[3] X Chen, R Adam, DE Bürgler, F Wang, Z Lu, L Pan, S Heidtfeld, C Greb, M Liu, Q Liu, J Wang, CM Schneider, D Cao. Ultrafast demagnetization in ferromagnetic materials: Origins and progress. In: *Physics Reports* **1102** (2025). Ultrafast demagnetization in ferromagnetic materials: Origins and progress, pp. 1–63.

[4] W Wu, C Yaw Ameyaw, MF Doty, MB Jungfleisch. Principles of spintronic THz emitters. In: *Journal of Applied Physics* **130**.9 (Sept. 2021), p. 091101.

[5] VK Mag-usara, MC Escaño, CE Petoukhoff, G Torosyan, L Scheuer, J Madéo, J Afalla, ML Talara, JE Muldera, H Kitahara, DR Bacon, M Nakajima, K Dani, ET Papaioannou, R Beigang, M Tani. Optimum excitation wavelength and photon energy threshold for spintronic terahertz emission from Fe/Pt bilayer. In: *iScience* **25**.7 (2022), p. 104615.

[6] Materials Project. *Materials Data on Ni (sg: 225) by Materials Project*. Licensed under CC BY 4.0. 2020.

[7] B Koopmans, G Malinowski, F Dalla Longa, D Steiauf, M Fähnle, T Roth, M Cinchetti, M Aeschlimann. Explaining the paradoxical diversity of ultrafast laser-induced demagnetization. In: *Nature Materials* **9**.3 (2010), pp. 259–265.

[8] Materials Project. *Materials Data on Pt (sg: 225) by Materials Project*. Licensed under CC BY 4.0. 2020.

[9] JH Shim, AA Syed, JI Kim, HG Piao, SH Lee, SY Park, YS Choi, KM Lee, HJ Kim, JR Jeong, JI Hong, DE Kim, DH Kim. Role of non-thermal electrons in ultrafast spin dynamics of ferromagnetic multilayer. In: *Scientific Reports* **10**.1 (2020), p. 6355.

[10] Materials Project. *Materials Data on Fe (sg: 229) by Materials Project*. Licensed under CC BY 4.0. 2020.

[11] M Battiato, K Carva, PM Oppeneer. Superdiffusive spin transport as a mechanism of ultrafast demagnetization. In: *Physical Review Letters* **105**.2 (2010), p. 027203.

[12] *Mantis Laser Operator's Manual*. Coherent Inc. 2008.

[13] DE Spence, PN Kean, W Sibbett. 60-fsec pulse generation from a self mode-locked Ti:sapphire laser. In: *Optics Letters* **16**.1 (1991), pp. 42–44.

[14] M Kuznetsov, F Hakimi, R Sprague, A Mooradian. High-power (¿0.5-W CW) diode-pumped vertical-external-cavity surface-emitting semiconductor lasers with circular TEM/sub 00/ beams. In: *IEEE Journal of Selected Topics in Quantum Electronics* **5**.3 (1999), pp. 561–573.

[15] Coherent. *OPSL Advantages Whitepaper Series #1: Wavelength Flexibility*. https://www.coherent.com/web-resources/white-paper/opsl-wavelength-flexibility-wp. Accessed: 2026-05-11.

[16] R Boyd. *Nonlinear Optics*. Academic Press, 2020.

[17] B Saleh, M Teich. *Fundamentals of Photonics*. Wiley Series in Pure and Applied Optics. Wiley, 2019.

[18] *RegA Model 9050 Laser Operator's Manual*. Coherent Inc. Apr. 2002.

[19] *Verdi V12 Laser Operator's Manual*. Coherent Inc. Sept. 2008.

[20] D Strickland, G Mourou. Compression of amplified chirped optical pulses. In: *Optics Communications* **56**.3 (1985), pp. 219–221.

[21] *Delta Single Shot Autocorrelator Operation Manual*. MiniOptic Technology Inc. Apr. 2003.

[22] *User's Guide Model 32 and 32B Cryogenic Temperature Controller*. Cryogenic Control Systems, Inc. Mar. 2008.

[23] M Seo, H Yamaguchi, AD Mohite, S Boubanga-Tombet, JC Blancon, S Najmaei, PM Ajayan, J Lou, AJ Taylor, RP Prasankumar. Ultrafast optical pump-probe spectroscopy of 2D materials. In: *Scientific Reports* **6**.1 (2016), pp. 1–9.

[24] M Born, E Wolf. *Principles of Optics: Electromagnetic Theory of Propagation, Interference and Diffraction of Light*. Cambridge University Press, 2013.

[25] M Surýnek, V Saidl, Z Kašpar, V Novák, RP Campion, P Wadley, P Němec. Investigation of magnetic anisotropy and heat dissipation in thin films of compensated antiferromagnet CuMnAs by pump–probe experiment. In: *Journal of Applied Physics* **127**.23 (June 2020), p. 233904.

[26] A Block, M Liebel, R Yu, M Spector, Y Sivan, FJG de Abajo, NF van Hulst. Tracking ultrafast hot-electron diffusion in space and time by ultrafast thermomodulation microscopy. In: *Science Advances* **5**.5 (2019), eaav8965.

[27] A Chauhan, S Sahu, P Ghosh, D Singh, SG Nath, A Kumar N. M., PK Panigrahi, C Mitra, N Kamaraju. Ultrafast dynamics of carriers, coherent acoustic phonons, and strain pulses in $BiSbTe_{1.5}Se_{1.5}$ topological insulator thin films. In: *Phys. Rev. B* **112** (5 Aug. 2025), p. 054311.

[28] GD Tsibidis. Ultrafast dynamics of non-equilibrium electrons and strain generation under femtosecond laser irradiation of Nickel. In: *Applied Physics A* **124** (2018), p. 311.

[29] U Bierbrauer, P Maldonado, S Mathias, M Cinchetti, B Rethfeld, M Aeschlimann, PM Oppeneer. Ultrafast magnetization dynamics in nickel: impact of strain and correlations. In: *Journal of Physics: Condensed Matter* **29**.24 (2017), p. 244002.

[30] C Thomsen, HT Grahn, HJ Maris, J Tauc. Surface generation and detection of phonons by picosecond light pulses. In: *Phys. Rev. B* **34** (6 Sept. 1986), pp. 4129–4138.

[31] RHM Groeneveld, R Sprik, A Lagendijk. Femtosecond spectroscopy of electron-electron and electron-phonon energy relaxation in Ag and Au. In: *Phys. Rev. B* **51** (17 May 1995), pp. 11433–11445.

[32] S Kumar, A Nivedan, A Singh, et al. THz pulses from optically excited Fe-, Pt- and Ta-based spintronic heterostructures. In: *Pramana - Journal of Physics* **95** (2021), p. 75.

[33] G Torosyan, S Keller, L Scheuer, et al. Optimized Spintronic Terahertz Emitters Based on Epitaxial Grown Fe/Pt Layer Structures. In: *Scientific Reports* **8** (2018), p. 1311.

[34] K Kaleris, E Kaniolakis-Kaloudis, E Kaselouris, K Kosma, E Gagaoudakis, V Binas, S Petrakis, V Dimitriou, M Bakarezos, M Tatarakis, NA Papadogiannis. Efficient ultrafast photoacoustic transduction on Tantalum thin films. In: *Applied Physics A* **129** (2023).

[35] R Adam, D Cao, DE Bürgler, et al. THz generation by exchange-coupled spintronic emitters. In: *npj Spintronics* **2** (2024), p. 58.

[36] G Malinowski, N Bergeard, M Hehn, et al. Hot-electron transport and ultrafast magnetization dynamics in magnetic multilayers and nanostructures following femtosecond laser pulse excitation. In: *The European Physical Journal B* **91** (2018), p. 98.

Appendix A

SOP for Cryo-con Model 32

Here we detail the standard operation procedure (SOP) for using Cryo-con Model 32 temperature controller with Janis VNF-100 Cryostat.

A.1 Quick Start Guide (Basic Usage)

For normal operation using the pre-calibrated settings, follow these steps to initialize the temperature controller after one rotates the Flow valve (no more than 2 rotations) as per section A.3.

1. **Sensor Connection:** Connect the Janis cryostat A port to **Input B** on the Cryo-con controller using the standard Military Cable.
2. **Heater Connection:** Connect the two heater cables (Dual Banana Plug) from the Military cable into the **Loop 1** output on the back of the controller.
3. **Power On:** Turn on the Cryo-con Model 32.
4. **Select Table:** Navigate to the `Loop 1` (button 3) settings and ensure **Table 1** is selected. This table contains the pre-calculated PID values and heater range interpolations.
5. **Verify Input Source:** Ensure that the control input source for Loop 1 is set to **Input B** (the standard calibration input, under `Loop 1` settings itself).
6. **Set Temperature:** Press the `SETPT` button (+/-) to select the desired target temperature for Loop 1.
7. **Engage Control:** Press the `CONTROL` button to engage the heater loop. The PID controller will automatically adjust current based on the table settings to reach the temperature set as per `SETPT`.

A.2 System Configuration and Wiring Details

A.2.1 Rear Panel Connections

The Cryo-con Model 32 is wired as follows:

- **Input A:** BNC/Custom Sensor DIN43760/Pt100 (optional extra sensor).
- **Input B:** Primary Control Sensor via Military Cable (8 and 10 pins).
- **Loop 1:** Primary Heater (Dual Banana Plug).
- **Loop 2:** Secondary Heater (Terminal Block Plug).

A.2.2 Custom Sensor Integration (Input A)

A custom extra Pt100 sensor (DIN43760) has been installed to monitor temperature directly next to the sample. Input A usually works better with Aggressive PID, when using it for Loop 1 input with Janis.

Wiring Configuration

Based on the Cryo-con manual (Page 77), the extra sensor is connected using a 4-wire configuration:

- **Pins 1 & 2:** Shorted together (Jumpered).
- **Pins 4 & 5:** Shorted together (Jumpered).
- **Pin 3:** Left open (Shield).
- **Signal Connection:** The sensor leads are soldered to BNC which connects via jumper to Pins 1 and 4.

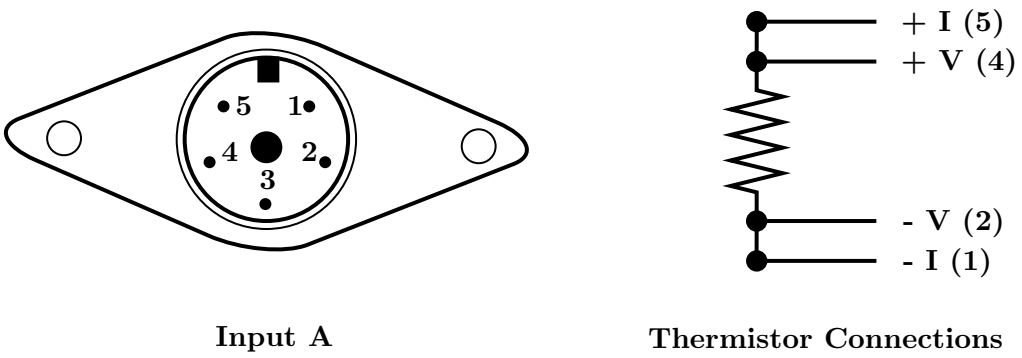

Figure A.1: Sensor Wiring Diagram (Refer to Cryo-con Manual Pg. 77 for more details)

Installation

The sensor is soldered to the BNC cable inside the Janis cryostat at the top of the sample holder rod with one terminal soldered to the body of the metal holder directly and the other sensor terminal soldered to the ferrule and positioned immediately adjacent to the sample location. A BNC-to-jumper adapter is used externally to route these connections to the Cryo-con Input A port.

Controller Setup

In the Cryo-con system menu:

1. Press the `SENSOR` key and Select the channel to configure (e.g., `Input A`).
2. Navigate to the **Sensor Type** field.Press `ENTER` to view the list and select: **DIN43760**.
3. Press `HOME` to return to the main screen.

A.3 Cooling and Flow Valve Dynamics

A.3.1 Initial Cooling

To reach the desired temperature, rotate the Liquid N_2 flow valve on the Janis to **a maximum of 2 rotations** (do not exceed this limit per manual).

As a general observation, for temperatures below 85K, liquid nitrogen must contact the metal sample holder. For temperatures below 77K, the sample must be fully submerged with continuous vacuum pumping of the sample chamber.

A.3.2 Advised Flow Rates

Use 2 rotations for temperatures below 90K, 1.5 rotations for temperatures between 90K-110K and 1 rotation for higher temperatures. Leave the flow valve at the appropriate setting and turn on the control button.

One should ideally monitor the liquid nitrogen level with a camera during measurements to avoid interupting readings.

A.3.3 Valve Jamming Issue

It has been observed that the flow valve tends to freeze or "jam" approximately **5 minutes** after cooling begins. This is indicated by a sudden, sharp decrease in the cooling rate in the live temperature plots (temperature drops much slower).

Temporary Correction: If this occurs, rotate the valve knob back and forth twice to clear the ice blockage and restore the original cooling rate during rapid cooling. However, this is not feasible while taking readings and prevents one from maintaining lower temperatures.

Prevent Blockage:, maintain the cryostat at 300K using the temperature controller when not in use and remove the nitrogen chamber lid, replacing it with tissue paper tied around the opening. This prevents contamination while allowing water to evaporate. This method has been verified twice, and either the tissue paper, maintaining 300K, or both are necessary to prevent water accumulation in the nitrogen dewar and avoid clogging the flow valve.

A.4 PID Tuning and Control Physics

The PID (Proportional-Integral-Derivative) parameters were determined using the **Ziegler-Nichols** closed-loop tuning method.

A.4.1 Tuning Process

A "PID Circle" was created by setting the system to oscillate at a stable amplitude around 95 K. The following critical values were measured:

- **Ultimate Gain (K_u):** 150 (The minimum P-value where stable oscillation occurred).
- **Ultimate Period (T_u):** 6.8 seconds (Time per oscillation).

A.4.2 Parameter Calculation

Based on K_u and T_u, the following PID sets were calculated. We utilize a slightly modified "Balanced" set for general operation as in Table A.1.

Table A.1: PID Parameter Calculations

Parameter	Formula	Calculated Value	Notes
Balanced / Standard (Used in Table 0)			
P	$0.4 \times K_u$	**60.0**	Conservative Gain
I	$0.8 \times T_u$	**5.44**	Integral Time
D	Fixed	**0.5**	Manually tuned for stability
Aggressive (Optional)			
P	$0.6 \times K_u$	90.0	Faster response
I	$0.5 \times T_u$	3.4	—
D	$0.85 \times T_u$	5.78	Unstable, but works for noisy env

A.4.3 Heater Range Configuration

These values are programmed into **Table 0** of the controller. The heater current ranges are interpolated automatically:

- **$<$ 85 K:** Heater Range set to **MID**.
- **$>$ 85 K:** Heater Range set to **HIGH**.

A.5 Automated Data Acquisition

A custom Python script (`cryo.ipynb`) was developed to log temperature data live. To use the same, connect a (ideally windows based) machine to Cryo-con via GPIB, and utilize VISA for remote controlling the machine.

A.5.1 Prerequisites

To run the automation software on a Windows laptop, ensure the following are installed:

1. **NI-VISA:** National Instruments VISA driver.
   [*link*: https://www.ni.com/en/support/downloads/drivers/download.ni-visa.html]
2. **IEEE NI-488.2 Driver:** For GPIB communication (using standard National Instruments GPIB), or download respective driver of the cable in use.
   [*link*: https://www.ni.com/en/support/downloads/drivers/download.ni-488-2.html]
3. **Python Environment:** Required libraries include `pyvisa`, `matplotlib`, `pandas`, and `numpy`, `IPython`, `asyncio`, `ipywidgets`.

A.5.2 Command Usage

One can use commands as described in Table A.2 either directly via the NI-VISA Interactive Control interface or using PyVISA in Python.

- **Direct Method:** Navigate to NI-VISA Interactive Control, double-click the relevant GPIB COM Port, and go to the Input/Output tab.
- **PyVISA Method:** Initialize connection and use the following commands for queries and writes:

Table A.2: Basic Commands for VISA I/O with Cryo-con.

Type	**Command**	**Expected Output**
Query	`*IDN?`	Name and version of the controller
Query	`INP B:TEMP?`	Temperature detected by Input B
Query	`LOOP 1:SETPT?`	Get target temperature for LOOP 1
Write	`LOOP 1:SETPT 100`	Set target temperature for LOOP 1
Write	`CONTROL`	Starts Control mode to reach target temp
Write	`STOP`	Stops Control mode to reach target temp

```
1
2   import pyvisa
3   rm = pyvisa.ResourceManager()
4   controller = rm.open_resource('GPIB0::12::INSTR')
5
6   temp_str = controller.query('INP B:TEMP?')  # query temperature
7   controller.write('CONTROL')  # start control mode
```